

ENERGY SCAVENGING FROM ELECTRIC POWER LINES

Orpheas Kypris

0629695

Summary

The feasibility of powering a wireless sensor by scavenging the energy from a magnetic field underneath a 3-phase line has been explored by evaluating the availability of energy due to the magnetic field and analyzing different induction coil configurations. The power transferred to a resistive load of $30\text{ k}\Omega$ using a coil of 500 turns, radial thickness of 5.12 mm , length of 20.48 mm, mean turn radius of 56 mm and a core of $\mu_r=5000$ is approximately 0.9 VA under a field of $30\text{ }\mu\text{T}$.

Contents

1	Introduction	3
2	Literature Review	5
2.1	Power Scavenging Methods for Monitoring Applications	5
2.1.1	Solar Panels	6
2.1.2	Inductive	6
2.1.3	Capacitive	6
2.2	Principles of Electromagnetism	7
2.2.1	Ampere's Law	7
2.2.2	Biot-Savart Law	7
2.2.3	Mutual Inductance	8
2.3	Magnetic Field in the Vicinity of Three-Phase Power Lines	9
3	Computation of the Magnetic Field Under a Three Phase Overhead Power Line	12
3.1	Aims of this Chapter	12
3.2	Assumptions and Simplifications	12
3.3	Derivation of Analytical Equations	13
3.4	Computer Simulation of the Magnetic Field	16
3.4.1	MATLAB Computation	16
3.4.2	SLIM Computation	18
3.5	Chapter Conclusions	18
4	Coil Design	25
4.1	Equations for Magnetic Flux and Induced Voltage	25
4.2	Circuit Equation	27
4.3	Self-Inductance of the Coil	29
4.3.1	Calculations for the Air-Cored Coil	32
4.3.2	FEMM Simulation	33

4.4	Apparent Power Output	34
5	Circuit Simulation	43
6	Conclusions	45
6.1	Future work	45
6.1.1	Coil Design Revision	45
6.1.2	Conditioning Requirements	46
7	Acknowledgements	49
8	Bibliography	50
A	Appendix	52

Chapter 1

Introduction

The present research project explores the possibility of utilizing the magnetic field emanating from three-phase overhead conductors in a substation to power a wireless link of relatively low power consumption. The prime motivator in this effort is to provide a 'free' source of power, in order to alleviate the need for a battery source that unavoidably runs out at frequent intervals and requires replacement. The objectives of this study are the following: to evaluate the feasibility of using such a scavenging device, with criteria the availability of scavengeable energy, the physical/dimensional limitations of the device itself, as well as the real power that would therefore be transferred to the load; also, very importantly, to develop a clear relationship between the aforementioned factors, to facilitate future work, especially for the case in which one or more parameters have changed due to the nature of the problem.

The first concept to be confronted is the availability of scavengeable energy, and for this particular problem analytical equations are developed for the magnetic field and are then evaluated with the help of a MATLAB algorithm, specifically coded to suit this problem, however allowing alterations in the input variables. Along with that, a finite element method simulation is run on SLIM, to compare and contrast the results; furthermore, the results are also compared with an analytical formula derived by other researchers on the subject. This comparison was performed with three different magnitudes of RMS currents flowing in the overhead conductors, namely 100, 500 and 1000 A. Because of the multitude of scavenging 'induction coil' types, the problem is constrained by defining that the coil is to be placed underneath the conductors, at a specific vertical distance from the conductors; its horizontal displacement relative to the conductors is also defined. Most importantly, though, two extreme magnitudes for the field are quoted, namely 30 and 100 μT ; the positions in the plane of the conductors these are situated at can then be devised from the corresponding graphs for the magnetic field contour lines.

Through the usage of a script written in LUA language and run in FEMM 4.0, the dimensions of the coil are swept through from minimum to maximum values set by the author, in order to output inductance and resistance values for each configuration; this facilitates determining the most ideal configuration relative to physical properties, in order to decide upon a complete circuit later on.

Power output of the coil without and with two different loads connected is graphed and two magnetic cores with different magnetic permeabilities are chosen; that is for the reader to picture the interrelation individual circuit properties have, and their effect on power output. A chosen circuit configuration is then simulated on B2Spice, and the power output of that is discussed upon. Last, power electronics the conditioning part of the circuit would involve are discussed and future work is commented upon.

Chapter 2

Literature Review

2.1 Power Scavenging Methods for Monitoring Applications

Monitoring systems employing wireless nodes is, inarguably, an area of interest on which both government and industry are investing considerable effort in recent years. Due to the mobility and autonomous nature these systems aim to have, great emphasis has to be placed on the ways in which to power them. A wide variety of energy sources are available to power a sensor: photonic (solar), kinetic, thermal (solar-heated objects, ambient air, ground terrain), electromagnetic (ambient radiation, oscillating fields emerging from power lines), capacitive (electric potential imposed by power lines) and autophagous (battery);¹ the latter is to be avoided, if a sensor needs to retain autonomy. Also, the environmental constraints dictate the source of energy that would be most beneficial to harvest in each case.

A photovoltaic application involves a statistical study of the sun's maximum and minimum luminosity (or power) per unit area, over a specific period of time; needless to say that locations in the vicinity of the equator are subject to way more lumens per unit area averaged over a year, than locations in the northern hemisphere. For kinetic scavenging methods, the matter to consider first is the availability of moving mechanical parts. When scavenging from thermal sources, similar to the solar case, one has to consider a maximum and minimum temperature, and again this will vary depending on the location. Electromagnetic energy scavenging from power lines, though, seems to be a slightly more predictable source, as currents flowing in conductors depend on the load and vary only in a relatively small percentage. In other words, the energy source is always present. The same applies to capacitive energy scavenging from power lines, where the overhead line voltage induces a potential between two parallel plates.

The conclusion is that for powering a wireless sensor in the environment of a substation, the most appropriate sources are three: Solar panels, Inductive and Capacitive.

2.1.1 Solar Panels

Dondi et al.² look into powering a low power consumption IEEE 802.15.4/ZigBee compliant device, of approximately 50mW power consumption when the microcontroller and RF circuit are active. They employ switching to increase the power output of the solar panel, which at the input stage provides an output voltage of approximately 3 V under typical working conditions. The maximum output power is quoted at 500 mW at a light intensity of 1000 W/m² and 25°C temperature. The efficiency of the circuit depends on the power collected by the PV panel, as well as the power consumption of the load. However, light intensity is a very variable factor, and will depend on location and weather conditions.

2.1.2 Inductive

Thomas et al. briefly look into the scavenging of energy from electric power lines. They mention the possibility of linking a wire coil 'induction antenna' where the coil encircles the conductor itself or as an 'air-gap' transformer placed in the immediate vicinity of the conductor.¹ They correlate power output with various factors, including number of turns N , the permeability of the core material as well as the area of the core. The following table relates various configurations and coil placements to their respective RMS power dissipation:¹

Table 2.1: Calculated power scavenged from induction antennas assuming: $f = 60$ Hz, $A=1$ cm², and $Z=1$ Ω¹

Coil Turns N	Core permeability μ_r (W At ⁻¹ m ⁻¹)	Distance, r (m)	Current, I (A)	Power, P (W)
1	$4\pi \times 10^{-7}$ (air core)	1	1	5.68×10^{-17}
1	$1000 \times 4\pi \times 10^{-7}$	1	1	5.68×10^{-11}
100	$1000 \times 4\pi \times 10^{-7}$	0.01	100	56.8
100	$1000 \times 4\pi \times 10^{-7}$	0.1	100	0.568
1000	$1000 \times 4\pi \times 10^{-7}$	1	10	0.00568

However, the coil and load in the above case are matched with impedance $Z=1$ Ω. No mention is made about different loading and non-matched source and load.

2.1.3 Capacitive

A decent study on scavenging energy from electric fields up to 20 kV/m has been published by Zhu et. al.³ A voltage difference is induced on two metallic plates under an open-circuit condition. Switching is used (connecting and disconnecting the plates) to maximize the charge extracted from a capacitance. The harvested energy is given by the expression:³

$$E = \frac{1}{2}CV^2 \quad (2.1)$$

where C is the value of the capacitance, and V is the voltage on the capacitor. According to Zhu et. al, the switching is a major factor in increasing the scavenging efficiency.³ The scavenged power, ultimately, holds a

value of a few orders of magnitude less than 15.68 W; However, the dimension of the scavenging plate and the assessment of power that will go through a specific load is still a matter being looked into.³

2.2 Principles of Electromagnetism

2.2.1 Ampere's Law

As one of the most fundamental laws of electromagnetism, Ampere's law provides the basis for calculating the field in the vicinity of a current-carrying loop^{4(p225)}. It's derivation relies on the fundamental electromagnetic relationship, Maxwell's equation $\nabla \times \mathbf{B} = \mu_0 \mathbf{J}$, where \mathbf{B} is the magnetic field, and \mathbf{J} is the current density. Taking an area integral on both sides of Maxwell's law, one yields:

$$\int_S (\nabla \times \mathbf{B}) \cdot d\mathbf{S} = \mu_0 \int_S \mathbf{J} \cdot d\mathbf{S} \quad (2.2)$$

By definition of Stoke's theorem^{4(p34)}:

$$\oint_S \mathbf{F} \cdot d\mathbf{l} = \int_S (\nabla \times \mathbf{F}) \cdot d\mathbf{S} \quad (2.3)$$

Where $\nabla = \frac{d}{dx}, \frac{d}{dy}, \frac{d}{dz}$ and is the vector operator referred to as 'nabla'. Stoke's theorem states that for any vector field, the integral over the curl of an area equals the line integral around a closed loop. Since the integral of current density over an area equals the total current in that area I , the aforementioned relations will yield:

$$\oint \mathbf{B} \cdot d\mathbf{l} = \mu_0 I \quad (2.4)$$

Equation 2.4 is known as Ampere's Law.

2.2.2 Biot-Savart Law

Ampere's Law can serve as a starting point from which one can derive the Biot-Savart Law, another very important expression, which is utilized to calculate the magnetic field that arises from currents flowing in thin wires in free space. In this research project it is of utmost importance, as the analytical section of Chapter 3 relies exclusively on its application. The Biot-Savart law is analogous to the expression for the macroscopic electric field; to summarize, it divides a wire into an infinite number of elementary lengths, of which the sum of contributions will give the magnetic field at a point in space. The expression for the contribution of the magnetic field at point P arising due to an infinitesimal current element in a conductor of infinitesimal cross-section in free space is^{5(pp137–138)}:

$$d\mathbf{B}(P) = \frac{\mu_0}{4\pi} \frac{Id\mathbf{l} \times (\mathbf{r} - \mathbf{r}')}{|\mathbf{r} - \mathbf{r}'|^3} \quad (2.5)$$

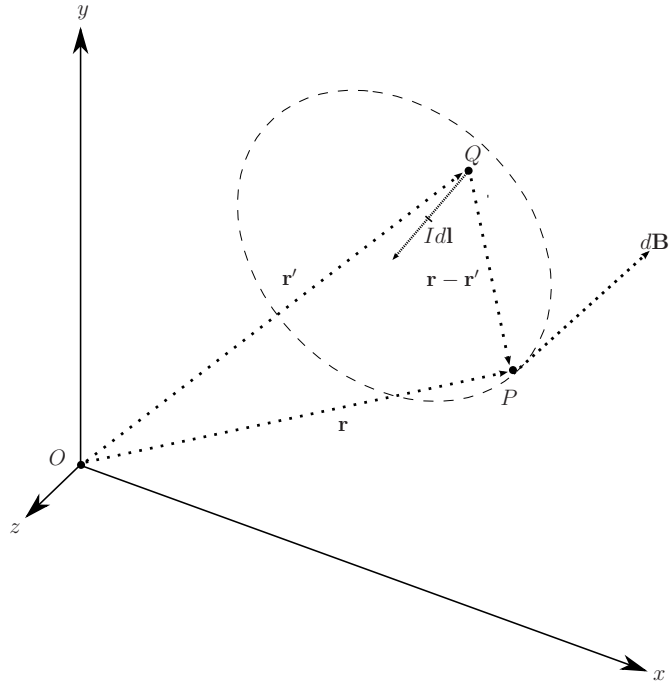


Figure 2.1: 3-dimensional illustration of the Biot-Savart law.

where μ_0 is the permeability of free space, Idl is an infinitesimal current element flowing along a straight section of the conductor, \mathbf{r} is the position vector from the origin to point P , and \mathbf{r}' is the position vector from the origin to point Q , as depicted in Figure 1. It is evident that the contribution $d\mathbf{B}$ is perpendicular to the current element Idz .

2.2.3 Mutual Inductance

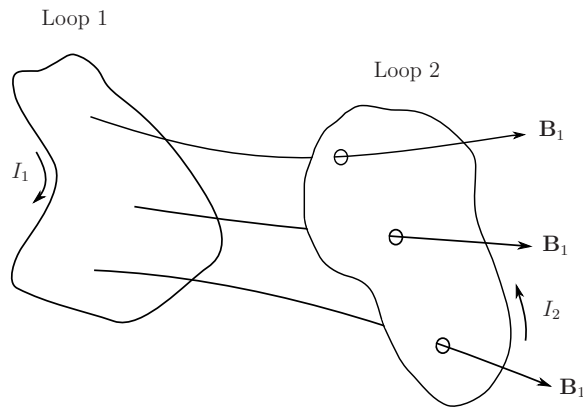


Figure 2.2: Mutual inductance between two loops.

By examination of Equation 2.5, it is evident that the field \mathbf{B} is proportional to the current I . Let the source of this field be a current I_1 flowing in loop 1, producing a field \mathbf{B}_1 as in Figure 2.2^{4(p311)}. If a loop 2 is placed anywhere in that field, let the flux through that loop due to the field \mathbf{B}_1 be denoted as Φ_2 . By looking at the Biot-Savart Law in Equation 2.5, if \mathbf{B} is proportional to I , \mathbf{B}_1 is proportional to I_1 ^{4(pp310–311)}. Consequently,

Φ_2 will then be proportional to I_1 , such that:

$$\Phi_2 = \int \mathbf{B}_1 \cdot d\mathbf{S}_2 \quad (2.6)$$

One can then deduce the proportionality constant M_{21} :

$$\Phi_2 = M_{21}I_1 \quad (2.7)$$

For deriving the formula for mutual inductance, Stoke's theorem is invoked:

$$\Phi_2 = \int \mathbf{B}_1 \cdot d\mathbf{S}_2 = \int (\nabla \times \mathbf{A}_1) \cdot d\mathbf{S}_2 = \oint \mathbf{A}_1 \cdot d\mathbf{l}_2 \quad (2.8)$$

Poisson's Equation (going to zero at infinity):

$$\mathbf{A}(\mathbf{r}) = \frac{\mu_0}{4\pi} \int \frac{J(r')}{r} d\tau' \quad (2.9)$$

According to the above equation:

$$\mathbf{A}_1 = \frac{\mu_0}{4\pi} I_1 \oint \frac{d\mathbf{l}_1}{r} \quad (2.10)$$

Hence:

$$\Phi_2 = \frac{\mu_0 I_1}{4\pi} \oint \oint \frac{d\mathbf{l}_1 d\mathbf{l}_2}{r} \quad (2.11)$$

Then, the Neumann Formula will result:

$$M_{21} = \frac{\mu_0}{4\pi} \oint \oint \frac{d\mathbf{l}_1 d\mathbf{l}_2}{r} \quad (2.12)$$

where M_{21} is the constant of proportionality, or the mutual inductance of the two loops. This scalar quantity is a function solely of the geometrical properties of a circuit, more specifically the size, shape and relative positions of the two loops. Also, the reciprocity theorem states that the mutual inductance of loop 1 due to loop 2 is identical to that of loop 2 due to loop 1, such that:

$$M_{21} = M_{12} \quad (2.13)$$

2.3 Magnetic Field in the Vicinity of Three-Phase Power Lines

In substations, the spatial configuration of busbars varies from one distribution company to another, depending on many variables which influence phase spacing and would therefore be considered by the substation design

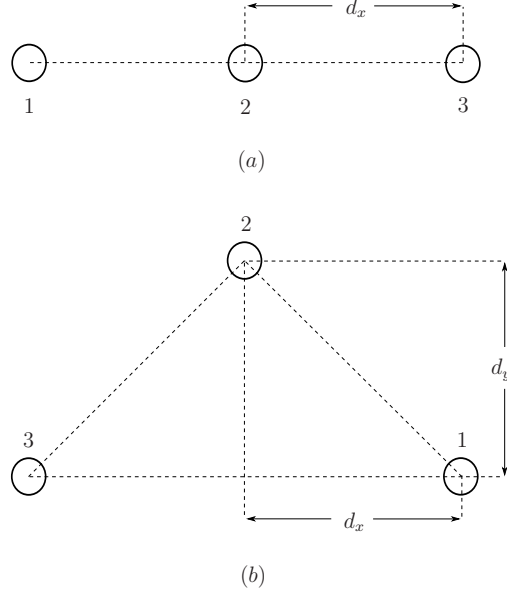


Figure 2.3: Two typical conductor arrangements

(a) depicts a single-circuit line with aligned conductors. (b) depicts a single-circuit line with triangularly arranged conductors. d_x and d_y are horizontal and vertical displacements relative to the individual conductors, while numbers indicates phases.

engineer; prior to the discussion of those factors, however, it has to be pointed out that the present study deals exclusively with tubular rigid busbars as opposed to strain busbars. With that in mind, one can deduce consistent conclusions regarding the magnetic field surrounding those conductors, since their spatial positioning is non-variable, with natural elements such as wind not influencing their relative positions.

Various bus configurations exist, namely the single bus and double bus arrangements. In a three-phase system, the first configuration involves solely a single direction for current flow, whereas the latter includes a return path for the current and therefore numbers six conductors in total. Magnetic field intensities, consequently, would differ for the two and that is why for the analysis of the magnetic fields in this study the first configuration was chosen, although one could easily adapt the problem to the second configuration.

Still, if one considers a single-line arrangement, different spatial configurations exist, depicted in Figure 2.3. Figure 2.3 (a) depicts an aligned arrangement, and 2.3 (b) depicts a triangle arrangement. However, substation design is a multi-decision, iterative process which involves variables such as ampacity requirements, corona and radio interference voltage, allowable stress on the conductors and physical constraints. Also, sufficient spacing must be provided in order to reduce the risk of flashover between phase to phase and phase to ground. Therefore, conductor spacing differs from case to case. For this study it was considered wise to allow 3 m for d_x and 6 m from ground to the conductor plane. Therefore, although the present study deals with the placement of the scavenging device in the vicinity of one particular busbar arrangement in a substation, the problem with its accompanying analytical equations and code can be altered to suit the magnetic field produced by a different arrangement.

Expressions for the magnetic produced by the specific configurations depicted in 2.3 are presented by Moro and Turri.⁶ Namely, an expression for the magnetic field strength produced by an aligned conductor arrangement

is:

$$b(R) = \frac{3}{\sqrt{2}} \frac{\mu_0 I}{2\pi} \sqrt{\frac{s^4 + s^2 R^2}{s^6 - 2R^3 s^3 \cos 3\phi + R^6}} \quad (2.14)$$

where in Figure 2.3 (a) $s = d_x$, R is the radial distance from phase 2 (the origin), and ϕ is the field point direction with the horizontal axis as reference. This expression will prove useful in comparing with the analytical expression derived in the relevant chapter of this study.

Chapter 3

Computation of the Magnetic Field Under a Three Phase Overhead Power Line

3.1 Aims of this Chapter

Rotating magnetic fields are, inarguably, present everywhere in space. The infinite range of field magnitudes one could therefore assume as starting values when devising the physical arrangement in space as well as the dimensions for a coil of specific power output would produce an infinite set of possible answers. It follows that due to the desire for a practical outcome, the interconnection and interdependence of different procedures in the present research, the problem has to be constrained to a significant extent prior to its analysis.

This chapter aims to provide an accurate mathematical and visual description of the rotating magnetic field in the vicinity of 3-phase power lines in a substation. Consequently, it will define the spatial boundaries throughout which possible placements of the inductive coil can be realized, as well as provide the data set required by further design steps. The scope is to confine the final output to a minimum set of results, so as to alleviate the effort of handling very large amounts of raw data when designing the coil, while still being able to maintain a certain degree of flexibility.

3.2 Assumptions and Simplifications

Since the problem formulated here is a special case of the concept of a magnetic field generated by a current-carrying conductor, the idea has to be defined further by making certain decisions that will lift the problem from the theoretical and place it into the practical domain. More specifically, the number of high-current conductors and their physical arrangement in space with respect to ground are parameters decided upon as absolutes when formulating the problem. For the sake of producing an accurate model of the real situation, the problem is formulated such as to allow for variations in the overhead current and conductor spatial configurations. Before advancing to

the mathematical formulation of the problem, a few definitions have to be made. The spatial configurations of high-current conductors in a substation may vary, therefore the first statement made has to be in regard of their positions with respect to each other and ground. This research only considers a specific spatial configuration (aligned conductors), however, the equations derived leave space for alterations. Figure 3.1 depicts the arrangement of the three-phase conductors in a system of three-dimensional Cartesian coordinates, where the x and y directions denote horizontal and vertical displacement respectively. Assuming that the conductors stretch to infinity along the z -axis will prove useful when deriving the equations later on. More specifically, the spatial configuration places the conductors at a height of 6 metres above ground, and a spacing of 3 metres between them.

For convenience, and since the problem adheres to a symmetrical nature namely of three equally spaced conductors extending infinitely in the z -direction, the field magnitude is equal as the z -axis is traversed while remaining in the same position on the $x - y$ plane. Of course, it is only safe to take this assumption if the distance from the conductor at which the field is calculated is significantly smaller than the length of the conductor itself. Also, in a practical situation, the conductors don't extend infinitely into the z -direction.

3.3 Derivation of Analytical Equations

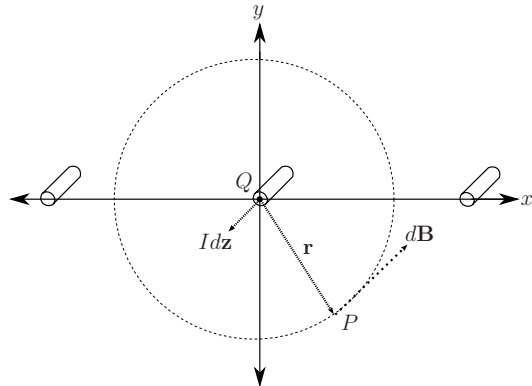


Figure 3.1: 2-D application of the Biot-Savart law.

Three aligned conductors with the 2nd phase contributing to $d\mathbf{B}$ with point Q (element $d\mathbf{z}$) now residing at the origin. Note that $d\mathbf{B}$ consists only of x and y components.

Consider a line configuration consisting of three horizontally aligned conductors, with the center of the middle conductor placed at the origin, as shown in Figure 3.1. If, in Equation 2.5, point Q is taken as the origin and assuming that the current element vector Idl consists only of a component in the z -direction (since the current flow is now out of the $x-y$ plane), the field can be written as:

$$d\mathbf{B}(P) = \frac{\mu_0}{4\pi} \frac{Id\mathbf{z} \times \mathbf{r}}{|\mathbf{r}|^3} \quad (3.1)$$

where Idz is an infinitesimal current element flowing in the z -direction and \mathbf{r} is the position vector from the origin (which is now the position of the current element Idz) to point P . However, since Equation 3.1 gives

the differential contribution from each current element to the magnetic field B at point P , an integration of the expression along $d\mathbf{z}$ is compulsory, if the total field at point P is desired. The cross-product of vectors $d\mathbf{z}$ and \mathbf{r} , ultimately giving the magnitude and direction of the magnetic field vector tangential to point P , is designated as follows:

$$d\mathbf{z} \times \mathbf{r} = \begin{vmatrix} \hat{\mathbf{B}}_x & \hat{\mathbf{B}}_y & \hat{\mathbf{B}}_z \\ 0 & 0 & dz \\ x & y & z \end{vmatrix} = -\hat{\mathbf{B}}_x(ydz) + \hat{\mathbf{B}}_y(xdz)$$

Substituting into 3.1 yields:

$$d\mathbf{B}(P) = \frac{\mu_0 I}{4\pi} \frac{-\hat{\mathbf{B}}_x(ydz) + \hat{\mathbf{B}}_y(xdz)}{|\mathbf{r}|^3} \quad (3.2)$$

Since \mathbf{r} , from the definition of the Biot-Savart law in cartesian co-ordinates, consists of $x^2 + y^2 + z^2$, and z approaches zero, consistent with the resultant field in this problem having only x and y components, the integral form can be expressed as follows:

$$d\mathbf{B}(P) = \frac{\mu_0 I}{4\pi} \left(-\hat{\mathbf{B}}_x y + \hat{\mathbf{B}}_y x \right) \int_{-\infty}^{\infty} \frac{dz}{\sqrt{x^2 + y^2}} \quad (3.3)$$

Integrating along dz :

$$\mathbf{B}(P) = \frac{\mu_0 I}{2\pi} \frac{-\hat{\mathbf{B}}_x y + \hat{\mathbf{B}}_y x}{x^2 + y^2} \quad (3.4)$$

One can consequently distinguish the x and y components of 3.4:

$$\mathbf{B}_x(P) = -\frac{\mu_0 I}{2\pi} \frac{y}{|\mathbf{r}|^2} \hat{\mathbf{B}}_x \quad (3.5)$$

$$\mathbf{B}_y(P) = \frac{\mu_0 I}{2\pi} \frac{x}{|\mathbf{r}|^2} \hat{\mathbf{B}}_y \quad (3.6)$$

The equations 3.5 and 3.6 can be modified further to allow for variations in the relative position, with respect to the origin, of a conductor in the $x - y$ plane. Substituting $x - d_x$ into x and $y - d_y$ into y :

$$\mathbf{B}_x(P) = -\frac{\mu_0 I}{2\pi} \frac{y - d_y}{(x - d_x)^2 + (y - d_y)^2} \hat{\mathbf{B}}_x \quad (3.7)$$

$$\mathbf{B}_y(P) = \frac{\mu_0 I}{2\pi} \frac{x - d_x}{(x - d_x)^2 + (y - d_y)^2} \hat{\mathbf{B}}_y \quad (3.8)$$

where d_x and d_y are the x and y co-ordinates of the desired conductor. In order to progress further, at this point it is necessary to define the individual currents carried by each one of the conductors in a three phase system. Abiding by the definition of a time-varying sinusoidal waveform, an expression for the current would be:

$$\vec{I}_n = I e^{j(\omega t + \phi_n)} \quad (3.9)$$

$$= I e^{j\omega t} e^{\phi_n} \quad (3.10)$$

with I being the peak value of the waveform, ω being the angular frequency and ϕ_n being the phase displacement of the n_{th} conductor. As the definition of a three phase power system dictates^{7(p24)}, balanced line currents lag each other by 120° , therefore it is imperative to define these as $\phi_1 = 0$, $\phi_2 = -\frac{2\pi}{3}$ and $\phi_3 = -\frac{4\pi}{3}$ for the first, second and third conductor respectively. The respective currents can then be written as follows:

$$\vec{I}_1 = I e^{j\omega t} e^{j(0)} \quad (3.11)$$

$$\vec{I}_2 = I e^{j\omega t} e^{j(-\frac{2\pi}{3})} \quad (3.12)$$

$$\vec{I}_3 = I e^{j\omega t} e^{j(-\frac{4\pi}{3})} \quad (3.13)$$

Now that the individual currents are defined, a logical progression would be to derive a magnitude for the field at point P due to the contribution of all three conductors. Note that since I is now a sinusoidal quantity, \vec{B} is a double vector quantity, varying both in space and time. For a system of n conductors, the principle of superposition can be applied, yielding the following sum:

$$\vec{B}(P) = \sum^n \vec{B}_n(P) \quad (3.14)$$

$$\vec{B}(P) = \sum^n \frac{\mu_0 \vec{I}_n}{2\pi} \frac{-\hat{B}_x(y - d_{y,n}) + \hat{B}_y(x - d_{x,n})}{(x - d_{x,n})^2 + (y - d_{y,n})^2} \quad (3.15)$$

The x and y components of the magnetic field at point P due to the contribution of more than one conductors become:

$$\vec{B}_{x,n}(P) = - \sum^n \frac{\mu_0 \vec{I}_n}{2\pi} \frac{y - d_{y,n}}{(x - d_{x,n})^2 + (y - d_{y,n})^2} \hat{B}_{x,n} \quad (3.16)$$

$$\vec{B}_{y,n}(P) = \sum^n \frac{\mu_0 \vec{I}_n}{2\pi} \frac{x - d_{x,n}}{(x - d_{x,n})^2 + (y - d_{y,n})^2} \hat{B}_{y,n} \quad (3.17)$$

Equations 3.16 and 3.17 become the basis of further calculations as well as in structuring the MATLAB code. It is now possible to formulate the equations for a system of $n = 3$ aligned conductors, with conductor 2 residing at the origin and the horizontal displacement of the conductors relative to each other being 3 metres.

The corresponding constants are therefore $d_{x,1} = -3$, $d_{y,1} = 0$, $d_{x,2} = 0$, $d_{y,2} = 0$, $d_{x,3} = 3$ and $d_{y,3} = 0$.

Substituting in Equations 3.16 and 3.17:

$$\vec{\mathbf{B}}_{x,total}(P) = -\frac{\mu_0 I e^{j\omega t}}{2\pi} \left(\frac{y}{(x+3)^2 + y^2} \hat{\mathbf{B}}_{x,1} + e^{j(-\frac{2\pi}{3})} \frac{y}{x^2 + y^2} \hat{\mathbf{B}}_{x,2} + e^{j(-\frac{4\pi}{3})} \frac{y}{(x-3)^2 + y^2} \hat{\mathbf{B}}_{x,3} \right) \quad (3.18)$$

$$\vec{\mathbf{B}}_{y,total}(P) = \frac{\mu_0 I e^{j\omega t}}{2\pi} \left(\frac{x+3}{(x+3)^2 + y^2} \hat{\mathbf{B}}_{y,1} + e^{j(-\frac{2\pi}{3})} \frac{x}{x^2 + y^2} \hat{\mathbf{B}}_{y,2} + e^{j(-\frac{4\pi}{3})} \frac{x-3}{(x-3)^2 + y^2} \hat{\mathbf{B}}_{y,3} \right) \quad (3.19)$$

Note that the term $Ie^{j\omega t}$ is a common factor to the sum, since all currents have the same magnitude and oscillate at the same frequency.

3.4 Computer Simulation of the Magnetic Field

The requirement to analyze the problem numerically, brought about two different and between them independent approaches. The first is a formulation of the problem in MATLAB code, serving several purposes: the calculation of field magnitudes at desired points in the $x - y$ plane, in order to facilitate plotting the vector fields around the three conductors and to produce graphs of displacement along the x axis versus field magnitudes for various constant positions on the y axis, as well as plots of B-field contour lines in the $x-y$ plane. Also, the output was used to produce tables of induced voltages for various coil configurations and positioning to later use in Microsoft Excel, for plotting purposes. The second method is characterized by a finite element method simulation carried out in the Areva SLIM Electromagnetic Engineering software package, a fully integrated collection of software modules that provides facilities for the generation and solution of electromagnetic finite element models.⁸ The results of both simulations can then be compared quantitatively.

3.4.1 MATLAB Computation

Since the operation of MATLAB⁹ relies in the most part on matrix algebra, the best approach towards devising an algorithm is considered to be one that uses matrices to store most, if not all outputs. Since the target of interest is a pre-defined boundary in the $x - y$ plane dictated by a nominal spatial configuration of three-phase conductors in a substation, all that is needed to throughput that information into matrix form is a discrete interval which will define the number of calculations along the x and y axes. Consistent with the fact that a 2-dimensional system of cartesian co-ordinates is employed, the result would be a $m \times n$ matrix, where m and n indicate co-ordinates in

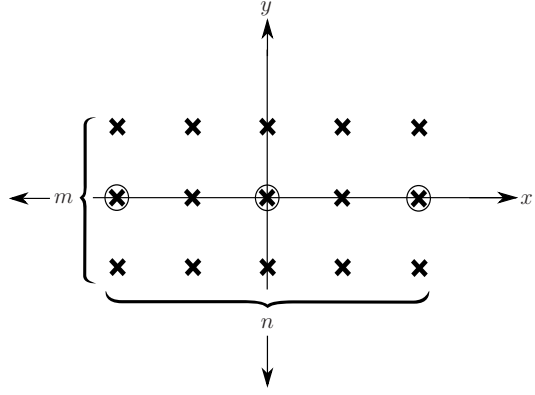


Figure 3.2: Visualization of the MATLAB algorithm.

The field contribution due to all three conductors is calculated at each point denoted by a cross and then stored in a matrix of dimensions $m \times n$, of which each element corresponds to a unique coordinate in the $x - y$ plane. The resolution of the mesh is specified by the user.

the $x - y$ plane 3.2. Along with the x and y boundary ranges, the calculation intervals along the x and y axes will ultimately set the m and n dimensions of the matrix respectively. Therefore,

$$m = \frac{y_2 - y_1}{\Delta y} \quad (3.20)$$

$$n = \frac{x_2 - x_1}{\Delta x} \quad (3.21)$$

where Δx and Δy represent the x and y axis calculation step intervals (or mesh resolution) respectively. Δx does not necessarily have to equal Δy , however for increased uniformity in the output (especially for the B-field magnitude plots), it is preferred. Also, y_2 and y_1 and x_2 and x_1 are the uppermost and lowermost limits on the y and x axes respectively, specifying the dimensions of the mesh. The individual field magnitudes at each point in the $x - y$ plane would then correspond to the matrix index yx . The storage algorithm implements a nested loop; the outer loop has a total iteration count of m , with a starting parameter of y_2 which is incremented by Δy to end at y_1 . The inner loop has a total iteration count of n , with a starting parameter of x_2 which is incremented by Δx to end at x_1 . Equations 3.18 and 3.19 reside in the inner loop and, on every iteration, each creates a new matrix entry with the index yx . Two matrices are produced (each of dimensions $m \times n$): The first contains the sum of the horizontal component of each \mathbf{B} at a point (three in this case), and similarly the second contains the sum of the vertical component of each \mathbf{B} at a point. Once the loop has exited, the Pythagorean theorem is applied to find the resultant magnitude of \mathbf{B} from its horizontal and vertical components, such as in:

$$\mathbf{B} = \sqrt{\mathbf{B}_x^2 + \mathbf{B}_y^2} \quad (3.22)$$

The result is stored into a new matrix which is used for plotting. To minimize memory requirements and processing time, Equations 3.18 and 3.19 are expressed in phasor notation, omitting the exponential term $e^{j\omega t}$.

The B-Field magnitude plots and contour line plots can be found in Figures 3.3 and 3.4 respectively. The code itself can be found in the Appendix.

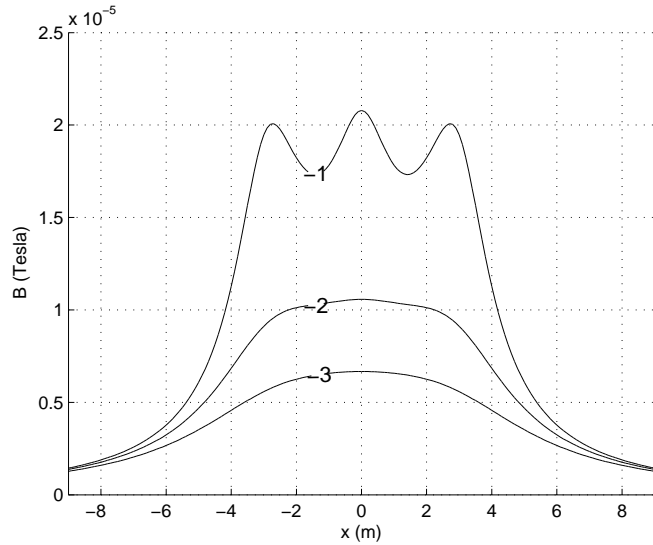
3.4.2 SLIM Computation

It would be a depthless and partial approach to the problem if one were to rely solely on analytical equations. Of course, the validity of Ampere's law is unquestionable; however, it was considered wise to simulate the problem using the finite element method. Although Ampere's law is, unavoidably, still the framework of calculations, the FEM simulation would go further than just expressing the magnitude of the field at a point with respect to the individual distances of three conductors from that point. The problem would be approached in a more realistic manner; the conductors are now modelled not as point charges, but as current carriers possessing a significant diameter (10 cm in this case) and material resistivity (copper). Furthermore, the simulation should also take into account the mutual inductance between the high-current conductors as well as the effect of ground. With these ideas in mind, the data sets resulting from the analytical calculations and the FEM simulation should not differ significantly, while expecting a small deviation.

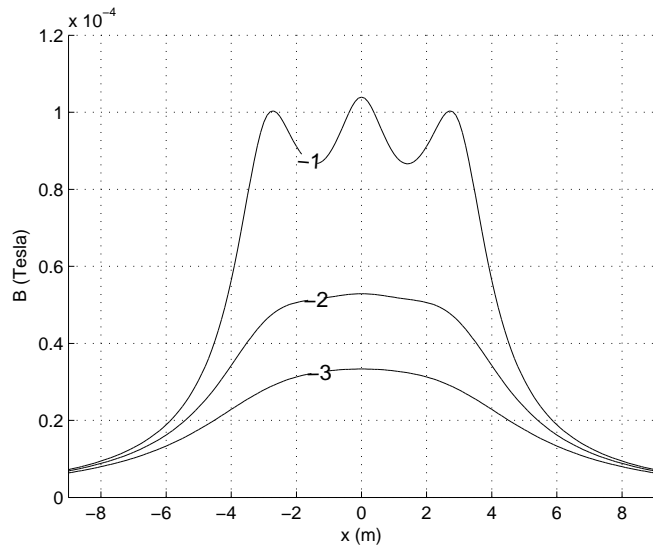
Consistent with the formulation of the problem in MATLAB, the mesh was designed via the SLIM 2D Mesh Generation GUI based module. Since the nature of the problem is symmetrical, the leftmost conductor and the left half of the middle conductor together with the air were designed, and the resulting mesh was mirrored and joined to produce the final, complete model (Figure 3.5(a)). The 2D Magnetodynamic data preparation module was employed to input the region/material properties (Figure 3.6(b)), the boundary conditions (where the boundary potentials were set to 0 as in Figure 3.6(a)) as well as to define the nodal and elemental data outputs necessary for the post-processing. Consequently, the 2D Magnetodynamic solver module was fed with the data preparation settings file, to produce an output suitable for post-processing. Three different control files were generated, each one for a different current in the overhead conductors. The 2D Post-Process module was then employed to produce the vector field display (Figure 3.5(b)), as well as the plots of horizontal displacement vs. field magnitudes (Figure 3.7). Using the mesh constructed for the magnetodynamic simulation, an electrodynamic simulation was carried out in order to evaluate the electric field between various points in the plane. This simulation serves in exploring whether or not a particular insulator (coil wire insulation) will withstand the potential difference if the coil is placed at a particular positioning in the x - y plane. The simulation results in Figure 3.8 are valid for a 275 kV line voltage and copper conductors.

3.5 Chapter Conclusions

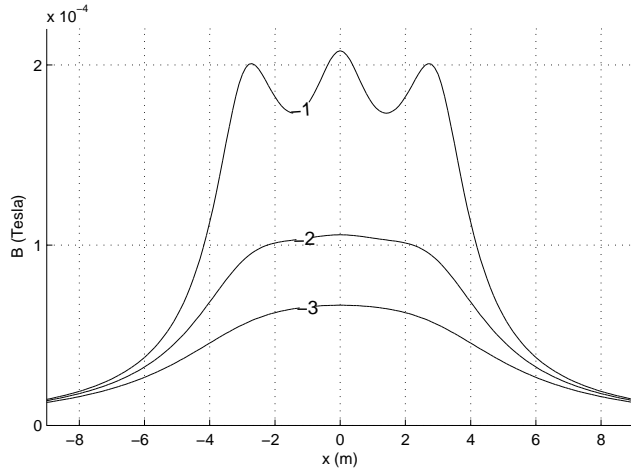
The plots of Figure 3.3 and Figure 3.7 differ slightly, as predicted, with the Matlab results having a higher magnitude. These deviations can be accounted for by the fact that the finite element method was constrained by a Dirichlet boundary condition where the tangential magnetic vector potential \mathbf{A} is set to 0 at the boundaries of the



(a) B-Field intensity in air for $I = 100 \text{ A}$

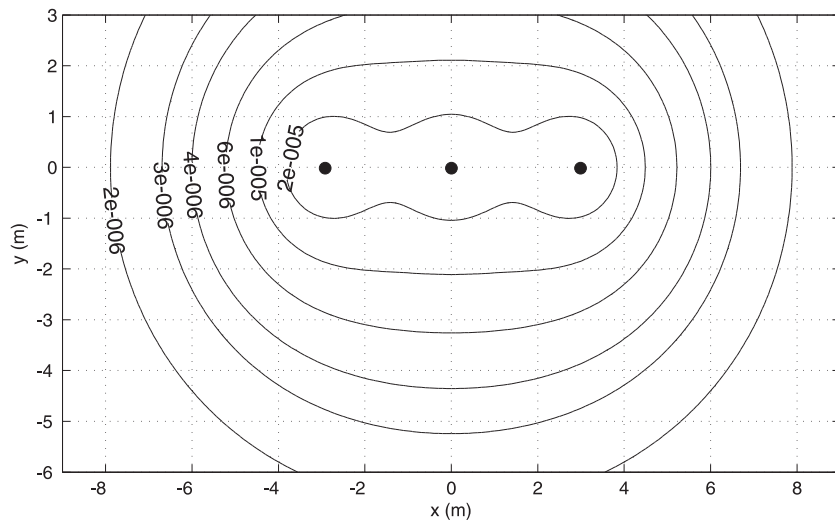


(b) B-Field intensity in air for $I = 500 \text{ A}$

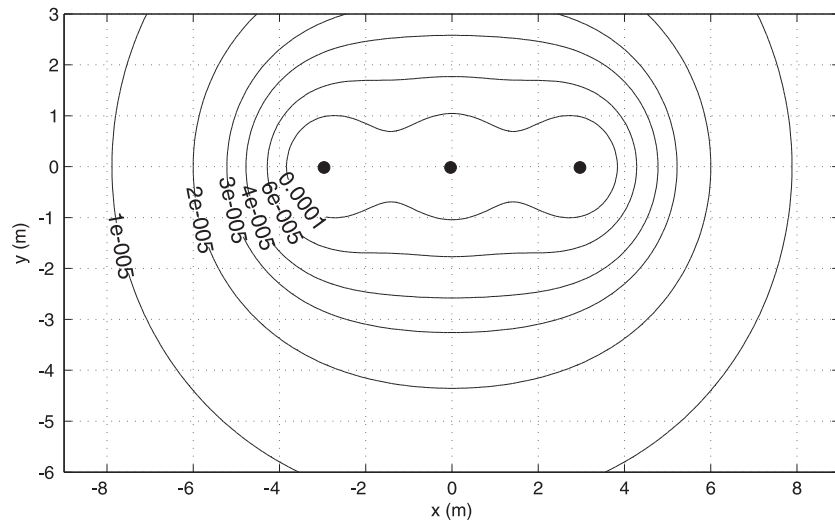


(c) B-Field intensity in air for $I = 1000 \text{ A}$

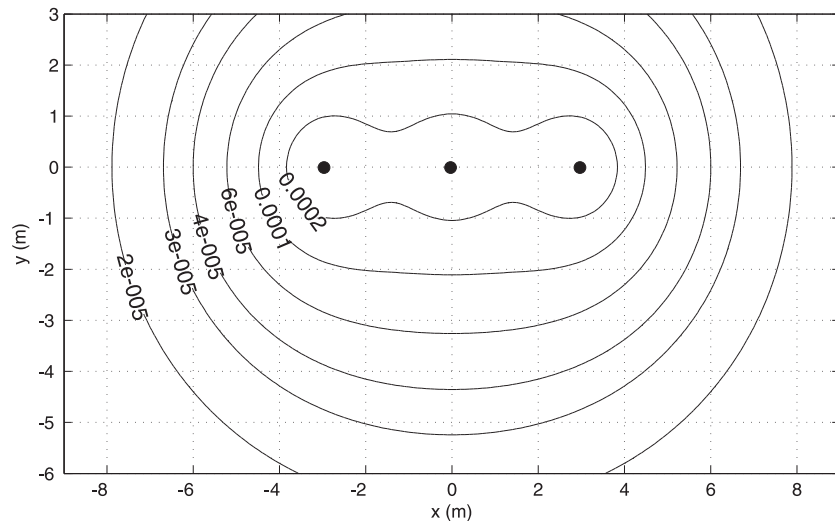
Figure 3.3: Matlab plots of B-Field in air (modulus of time and space) for varied currents in overhead conductors. Numbering on curves indicates y -displacement from $y = 0$. Phases 1,2 and 3 have coordinates of $(-3, 0), (0, 0)$ and $(3, 0)$ respectively.



(a) B-Field contours in air for $I = 100$ A

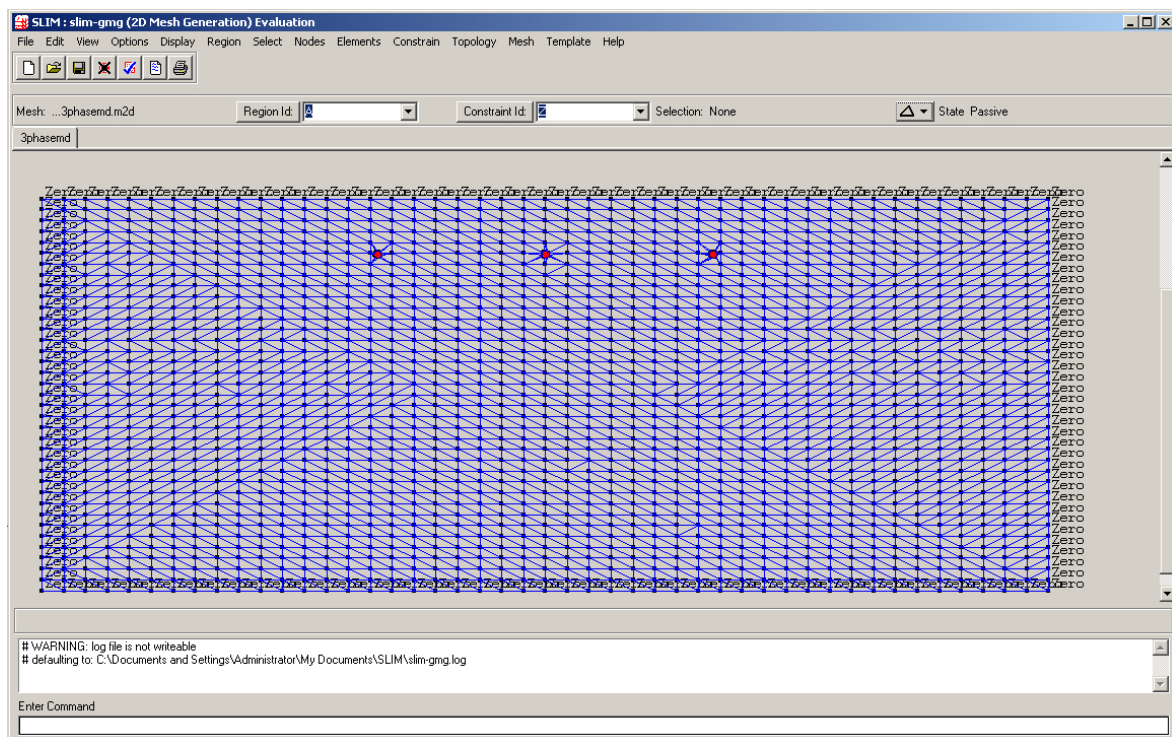


(b) B-Field contours in air for $I = 500$ A

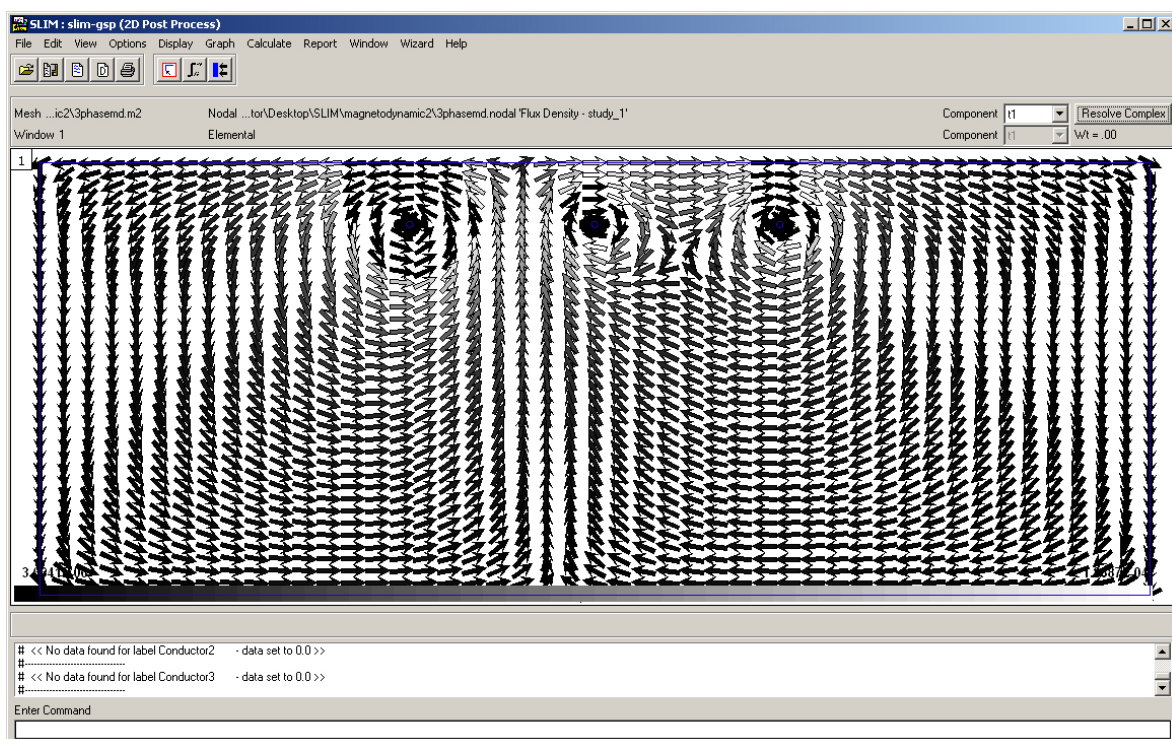


(c) B-Field contours in air for $I = 1000$ A

Figure 3.4: Matlab plots of B-Field contours air (modulus of time and space) for varied currents in overhead conductors. Numbering on curves indicates B-Field magnitudes in Tesla. Phases 1,2 and 3 have coordinates of $(-3, 0)$, $(0, 0)$ and $(3, 0)$ respectively.

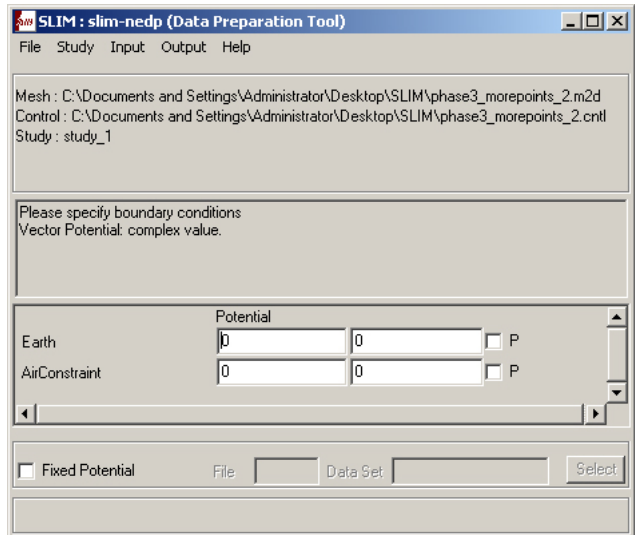


(a) SLIM 2D Mesh Generation GUI

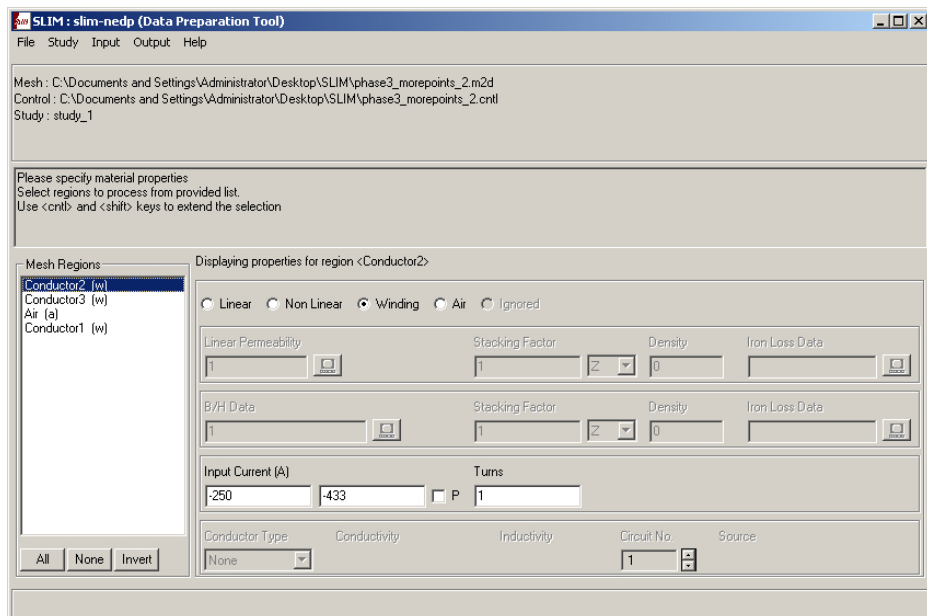


(b) SLIM 2D Post-Process GUI

Figure 3.5: 2D Mesh creation and graphical post-processing modules in SLIM.

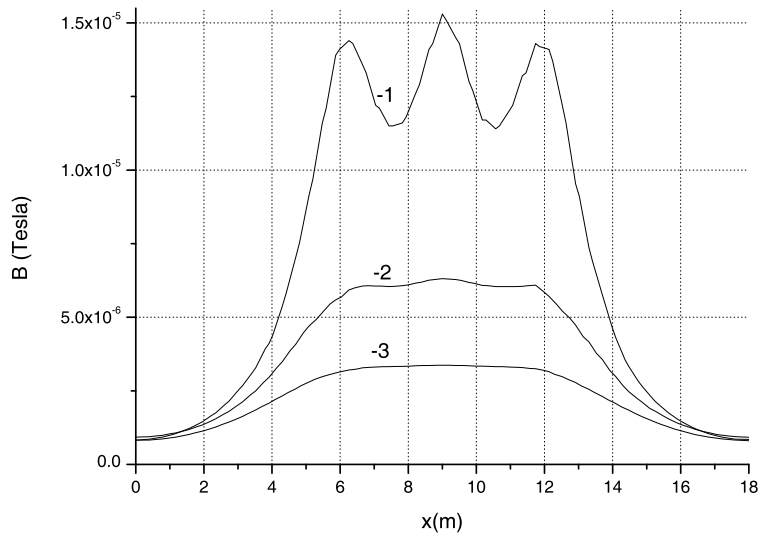


(a) SLIM Boundary Definition

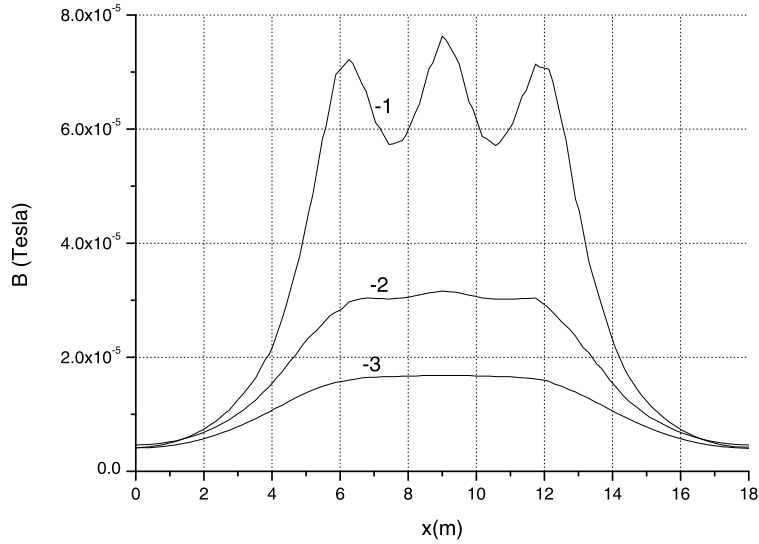


(b) SLIM Material Property Input

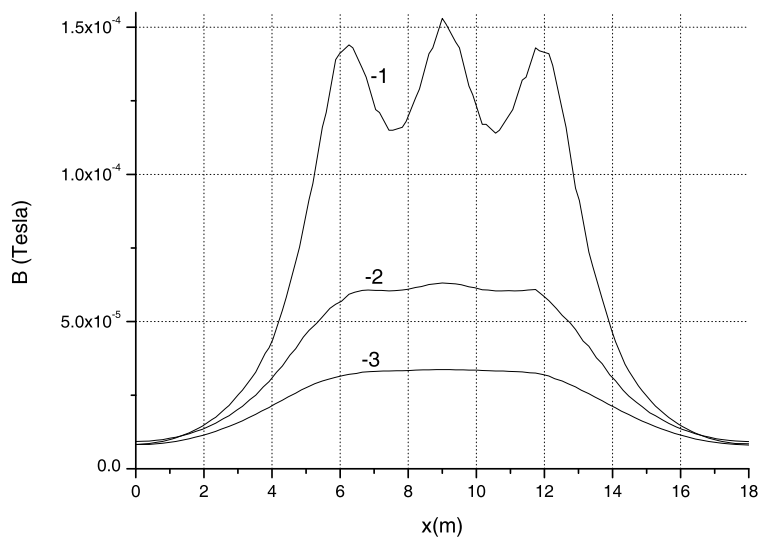
Figure 3.6: Data preparation windows for the 2D Magnetodynamic Solver module in SLIM.



(a) B-Field intensity in air for $I = 100 \text{ A}$

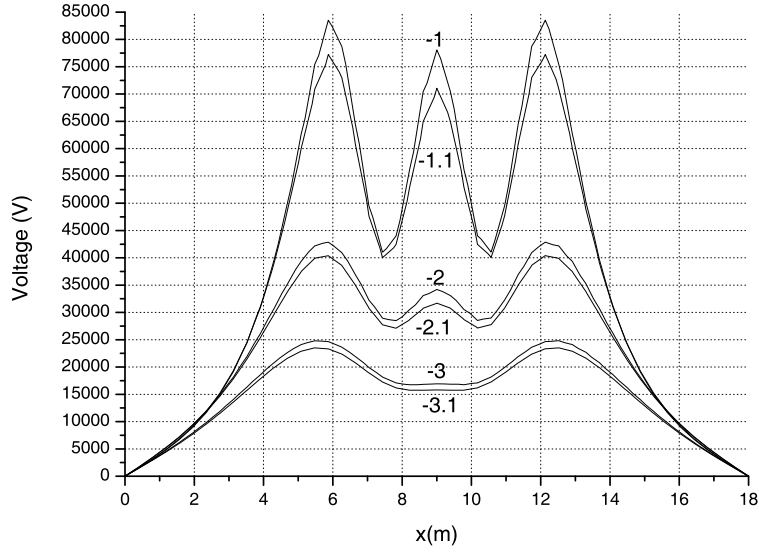


(b) B-Field intensity in air for $I = 500 \text{ A}$



(c) B-Field intensity in air for $I = 1000 \text{ A}$

Figure 3.7: SLIM plots of B-Field in air (modulus of time and space) for varied currents in overhead conductors. Numbering on curves indicates y -displacement from $y = 0$. Phases 1,2 and 3 have coordinates of $(6, 0), (9, 0)$ and $(12, 0)$ respectively.



(a) Potential difference in air at 275 kV

Figure 3.8: SLIM plot of potential difference (modulus of time) for 275 kV overhead conductors. Numbering on curves indicates y -displacement from $y = 0$. Phases 1,2 and 3 have coordinates of $(6, 0)$, $(9, 0)$ and $(12, 0)$ respectively.

mesh, thus having an effect on the magnetic field vector. To further verify the results, Equation 2.14 was used: points in the plane were converted from cartesian coordinates into spherical coordinates to be able to input them as R and ϕ . Also, s was set to 3 (the relative distances of conductors in this specific configuration). The results yielded were identical to the Matlab magnitude plots.

Chapter 4

Coil Design

4.1 Equations for Magnetic Flux and Induced Voltage

Having calculated the magnetic field via the simulations and analytical calculations, the total flux into an area can be found. From Faraday's law:

$$\Phi = \iint_S \vec{B} \cdot d\mathbf{S} \quad (4.1)$$

The three magnetic fields produced by three phase-displaced currents oscillating at the same frequency, can be summed, consistent with Equation 3.14:

$$\vec{B} = \vec{B}_1 + \vec{B}_2 + \vec{B}_3 \quad (4.2)$$

However, since the output of the MATLAB model is discretized to a user-defined resolution, with every point in the plane holding a magnitude for \vec{B} , way is given for a simplified approach to extract field magnitude data in order to design the coil, however not void of assumptions: The flux density vectors at two different points in the plane, are assumed to be of equal magnitude and direction (Figure 4.1), as long as the distance between those two points is significantly smaller than the distance between them and the current sources. Also, due to the elliptical nature of the field, it is assumed that where the coil is placed, $\vec{B}_x \gg \vec{B}_y$, so that $\vec{B} \cong \vec{B}_x$. Consequently, \vec{B} does not vary in space anymore in the chosen interval since the flux is assumed to cut the radial dimension of the coil orthogonally. \mathbf{S} becomes the scalar A since the angle between \vec{B} and $d\mathbf{S}$ is 0, and the flux is found by multiplying the derivative of \vec{B} by the area A :

$$\Phi = \vec{B}d\mathbf{S} \cos 0 \quad (4.3)$$

$$= \vec{B}A \quad (4.4)$$

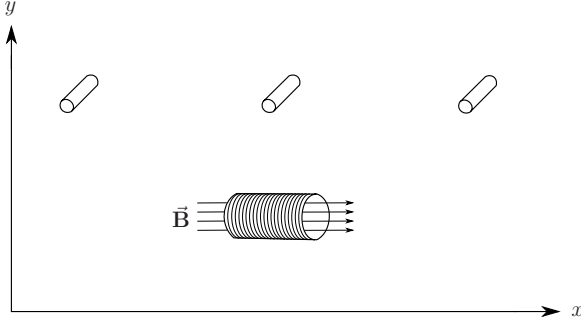


Figure 4.1: Coil placement in field.

The coil's axial dimension is parallel to the ground, and lines of \vec{B} are assumed to be identical over its radial dimension.

The voltage induced across the coil, from Faraday's Law^{5(p220)}, will be:

$$\vec{V} = -N \frac{d\Phi}{dt} = -N \frac{d\vec{B}}{dt} A \quad (4.5)$$

To differentiate with respect to time, one has to include the time variation (the Matlab output is expressed as a phasor). The derivative of the total flux density will then be:

$$\frac{d\vec{B}}{dt} = \frac{dB_1 e^{j\omega t}}{dt} + \frac{dB_2 e^{j\omega t}}{dt} + \frac{dB_3 e^{j\omega t}}{dt} \quad (4.6)$$

$$= j\omega (B_1 e^{j\omega t} + B_2 e^{j\omega t} + B_3 e^{j\omega t}) \quad (4.7)$$

$$= j\omega B e^{j\omega t} \quad (4.8)$$

To be able to utilize the Matlab output, however, this term needs to be converted to its phasor equivalent (of phase set to 0, as reference), which will be:

$$\frac{d\vec{B}}{dt} = j\omega B \quad (4.9)$$

To simplify, the modulus of the phasor in Equation 4.9 can be taken:

$$\left| \frac{d\vec{B}}{dt} \right| = \omega B \quad (4.10)$$

Substituting into Equation 4.5, the modulus of the voltage can be expressed as:

$$V = -N\omega BA \quad (4.11)$$

And if a magnetic core is added, Equation 4.11 becomes:

$$V = -\mu_r N\omega BA \quad (4.12)$$

4.2 Circuit Equation

Equation 4.12 alleviates the need to integrate along an area, fact that proved useful when producing tables of data for various field magnitudes and coil positionings later in the research. Another important idea that prevails is that since $\cos(0) = 1$, the flux and therefore the voltage induced across the coil are assumed to be maximum. Of course, the validity of this assumption is strengthened as the separation of the coil and the field source is increased, where $\vec{B} \cong \vec{B}_x$. Regarding the area A , for a coil of a square radial dimension it will equal d^2 , where d is the side of the square, and for a coil of a circular radial dimension it will equal πa^2 , where a is the mean radius of the turns. Figure 4.2 represents the two coil configurations.

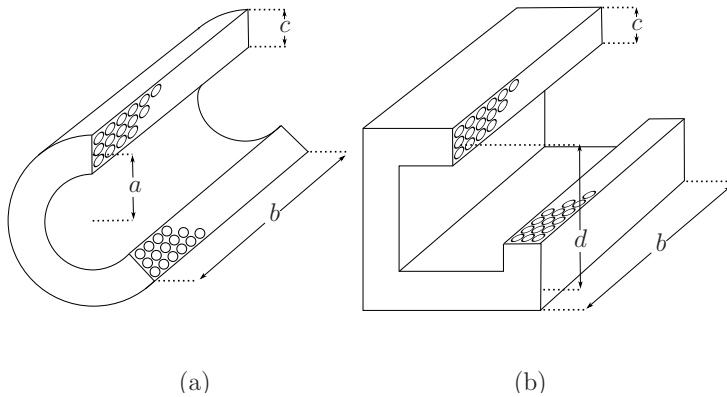


Figure 4.2: Two isometrically displayed coil configurations.

Both coils are of rectangular cross section b and thickness c , with (a) having a circular radial dimension a and (b) having a square side d . The circular shapes in the plane of the cross section indicate multiple layers of windings.

The placement of the coil in a magnetic field will induce a voltage across the ends of the coil, which will consequently initiate a current flow. That current flow, consistent with Lenz's law, will set up a voltage drop tending to oppose the externally induced voltage. This physical procedure is characterized by the self-inductance, which is the property of an electrical circuit where a change in the current flowing through that circuit induces a voltage that opposes the change in current. The block diagram of Figure 4.3 depicts an equivalent circuit model for the coil connected in series with a conditioning circuit and a load. For the time being, let us ignore the conditioning circuit; traversing the short-circuited coil in the positive direction, Kirchhoff's voltage law leads to:

$$E - L_C \frac{d\vec{I}}{dt} - R_C \vec{I} - \vec{Z}_L \vec{I} = 0 \quad (4.13)$$

Where E is the RMS voltage induced in the coil due to the magnetic field, and L_C and R_C are the self-inductance and resistance of the turns respectively. \vec{Z}_L is the impedance of the load. The $R_C \vec{I}$ term takes into account the d.c. resistance of the coil, from assuming that at low (power) frequencies the skin effect is negligible. R_C is a function of ρ , the resistivity of the wire medium, l , the length of the wire, as well as A_{wire} , the cross-sectional area of the wire itself, such that $R = \rho \frac{l}{A_{wire}}$. l is a function of the number of turns and radius of each turn, however for a coil such as in Figure 4.2 where $c \ll a$ it can be approximated that the radius of all turns is

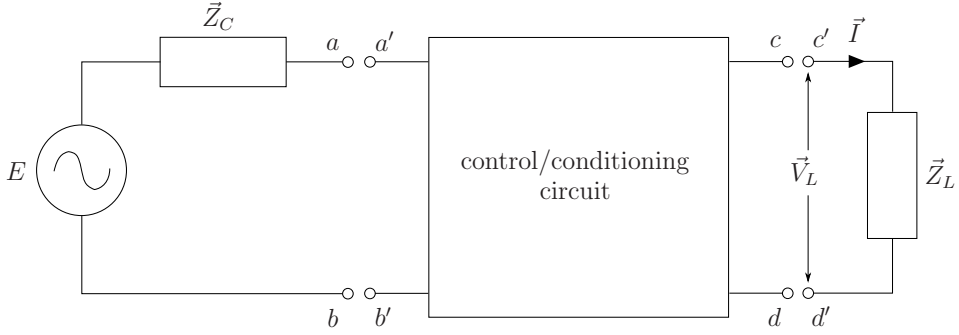


Figure 4.3: Model for the coil circuit.

Block diagram visualization of the final circuit, with the induced voltage represented by an AC source and the coil's resistance R_C and inductance L_C substituted by the total coil impedance \vec{Z}_C ; the load is represented by an impedance \vec{Z}_L . In between the coil and the load mediates a conditioning/control circuit.

equal, namely a , such that:

$$R = \rho \frac{2\pi a N}{\pi (d_{wire}/2)^2}. \quad (4.14)$$

Where d_{wire} is the diameter of the wire itself. Now, substituting equations

$$N\omega BA - L_C \frac{d\vec{I}}{dt} - R_C \vec{I} - \vec{Z}_L \vec{I} = 0 \quad (4.15)$$

Rearranging and evaluating the differential in phasor notation:

$$N\omega BA = L_C \frac{d\vec{I}}{dt} + R_C \vec{I} + \vec{Z}_L \vec{I} \quad (4.16)$$

$$= j\omega L_C \vec{I} + R_C \vec{I} + \vec{Z}_L \vec{I} \quad (4.17)$$

The current in the short-circuited coil will then be:

$$\vec{I} = \frac{-N\omega BA}{j\omega L + R_C + \vec{Z}_L} \quad (4.18)$$

To facilitate plotting, apparent power is chosen to be calculated first. Apparent power is the modulus of complex power. Complex power is denoted as:

$$\vec{S} = \vec{V}\vec{I}^* = \vec{P} + j\vec{Q} \quad (4.19)$$

And its modulus, apparent power is denoted as:

$$|\vec{S}| = S = \sqrt{P^2 + Q^2} \quad (4.20)$$

The product of modulus of voltage and the modulus of the current will also yield apparent power. For that, the modulus of I is taken, such that:

$$|\vec{I}| = I = \left| \frac{-N\omega BA}{j\omega L + R\vec{I} + \vec{Z}_L \vec{I}} \right| \quad (4.21)$$

When taking the load into account, the modulus of the voltage across it will be:

$$|\vec{V}_L| = V_L = E \left| \frac{\vec{Z}_L}{\vec{Z}_C + \vec{Z}_L} \right| \quad (4.22)$$

where $\vec{Z}_C = j\omega L + R_C$. The apparent power through the load is therefore $|V_L||I|$. However, apparent power is not an objective measurement of the power that is delivered to the load. Complex power, defined as $\vec{S} = \vec{P} + j\vec{Q}$, is a more accurate representation, with \vec{P} being real and \vec{Q} being imaginary, denoted by Watts and VAr respectively. Since \vec{Z}_C is known to have an imaginary part due to the inductive reactance of the coil and \vec{Z}_L is not likely to be purely resistive (as is the case with most practical loads), the real power delivered may vary, depending on the magnitudes of the resistances and reactances.

4.3 Self-Inductance of the Coil

Although the induced voltage is derived for a square shaped area of side d , the equivalent area covered by a circle of mean radius a would be valid, keeping in mind the assumptions stated in the beginning of the chapter. In order to now obtain the current flowing in the circuit, the value for self-inductance L has to be calculated. However, more specifications regarding the nature of the scavenging mechanism have to be made, bearing in mind that only in the absence of a magnetic material can an analytical equation retain its accuracy. In the case of air-cored circuits, the magnetic induction at any point due to a current I is directly proportional to that current. To complete the analogy, the voltage drop and current in the coil will be proportional to the total flux emanating from the three-phase conductors. Although the flux linkages of the coil with the three conductors individually will vary (due to the 120° phase difference), the total linkage with the conductors can be expressed as a constant times the current flowing in the coil. It is therefore imperative to first explore the possibility of employing a coil free of magnetic material before attempting to include a magnetic core. Still, since the intention is to include a magnetic material, the value for self-inductance has to be reconsidered accordingly; the non-linearity of the B-H curves of magnetic materials used in these types of applications, has to be approximated into being linear for the portion of the curve the field is going to be oscillating in (approximately $30 \mu T$ to $100 \mu T$ in air). L_C will therefore be multiplied by the constant μ_r , such that Equation 4.17 will change into:

$$\mu_r N \omega B A = (j\omega \mu_r L_C + R_C + \vec{Z}_L) \vec{I} \quad (4.23)$$

Therefore, the induced voltage in the coil is multiplied by the constant μ_r as in Equation 4.12, and in the

same manner is the self-inductance of the coil. Another notion in question is the physical dimension of the coil: a small, compact, lightweight configuration, which can easily be mounted onto a surge arrester and that will not disturb the arrangement of high-voltage apparatus in a substation; the least desired result is to establish a source of instability that would disturb power transmission, in terms of operation and safety. But again, a compromise between physical dimensions and power output of the coil has to be made, since the dimensions will effectively determine the inductance. More specifically, self-inductance for an air-cored coil is a function of the total number of turns N , axial length b as well as mean radius a or side d . If multiple layers rather than just a single layer of winding are to be employed, one has to consider the radial thickness c as well. This creates the need to define a further two parameters, namely number of turns in the axial direction N_b and number of turns in the radial direction N_c , such that $b = N_b d_{\text{wire}}$, $c = N_c d_{\text{wire}}$ and $N = N_b N_c$.

By observation, Equation 4.18 reveals that the current is inversely proportional to the self-inductance and resistance of the coil, while being directly proportional to the voltage induced across its ends. Therefore, there has to be a compromise between the nominator and denominator, such that the current is always maximum compared to the physical dimensions. The factors directly affecting this relationship, and which are inherent to the physical coil configuration, are the number of turns and the radial dimension of the coil. The induced voltage is a function of N and area A (as in Equation 4.5) determined by a or d , which are also factors in determining the self-inductance along with b and c . It follows that, if one wishes to find the golden ratio for this problem, he has to experiment with the latter two parameters. This is non-trivial, since countless different configurations exist. Thus, start and end values in terms of dimensional parameters and placement of the coil in the field have to be specified, in order to be able to progress in varying the rest of the parameters. Equation 4.12 enables the tabulation of induced voltages for varying N and a , to serve as a guideline and tool to calculate the current and consequently, the power the coil will output. Displayed in Tables 4.1, 4.2, 4.3 and 4.4, are values of induced voltages for various coil configurations and positionings in the field, calculated via a custom-made spreadsheet in Microsoft Excel.¹⁰ The ranges of N and a are, according to the author, the most practically realizable configurations. Figure 4.8 on page 39 is a graphical representation of Tables 4.1 and 4.3. Notice that the trend is linear.

Table 4.1: Induced Voltages E for $30 \mu\text{T}$, $\mu_r = 5000$

a (mm)	d (mm)	N				
		100	200	300	400	500
5.64	10	0.47	0.94	1.4	1.87	2.34
11.28	20	1.87	3.74	5.62	7.49	9.36
16.93	30	4.21	8.43	12.64	16.85	21.06
22.57	40	7.49	14.98	22.47	29.96	37.45
28.21	50	11.7	23.4	35.11	46.81	58.51
33.85	60	16.85	33.7	50.55	67.41	84.26
39.49	70	22.94	45.87	68.81	91.75	114.68
45.14	80	29.96	59.92	89.87	119.83	149.79
50.78	90	37.92	75.83	113.75	151.66	189.58
56.42	100	46.81	93.62	140.43	187.24	234.05

Table 4.2: Induced Voltages E for $100 \mu\text{T}$, $\mu_r = 5000$

a (mm)	d (mm)	N				
		100	200	300	400	500
5.64	10	1.57	3.14	4.71	6.28	7.85
11.28	20	6.28	12.57	18.85	25.13	31.42
16.93	30	14.14	28.27	42.41	56.55	70.69
22.57	40	25.13	50.27	75.4	100.53	125.66
28.21	50	39.27	78.54	117.81	157.08	196.35
33.85	60	56.55	113.1	169.65	226.19	282.74
39.49	70	76.97	153.94	230.91	307.88	384.85
45.14	80	100.53	201.06	301.59	402.12	502.65
50.78	90	127.23	254.47	381.7	508.94	636.17
56.42	100	157.08	314.16	471.24	628.32	785.4

Table 4.3: Induced Voltages E for $30 \mu\text{T}$, $\mu_r = 30000$

a (mm)	d (mm)	N				
		100	200	300	400	500
5.64	10	2.81	5.62	8.43	11.23	14.04
11.28	20	11.23	22.47	33.7	44.94	56.17
16.93	30	25.28	50.55	75.83	101.11	126.39
22.57	40	44.94	89.87	134.81	179.75	224.69
28.21	50	70.21	140.43	210.64	280.86	351.07
33.85	60	101.11	202.22	303.33	404.44	505.55
39.49	70	137.62	275.24	412.86	550.48	688.1
45.14	80	179.75	359.5	539.25	719	898.75
50.78	90	227.5	454.99	682.49	909.98	1137.48
56.42	100	280.86	561.72	842.58	1123.43	1404.29

Table 4.4: Induced Voltages E for $100 \mu\text{T}$, $\mu_r = 30000$

a (mm)	d (mm)	N				
		100	200	300	400	500
5.64	10	9.42	18.85	28.27	37.7	47.12
11.28	20	37.7	75.4	113.1	150.8	188.5
16.93	30	84.82	169.65	254.47	339.29	424.12
22.57	40	150.8	301.59	452.39	603.19	753.98
28.21	50	235.62	471.24	706.86	942.48	1178.1
33.85	60	339.29	678.58	1017.88	1357.17	1696.46
39.49	70	461.81	923.63	1385.44	1847.26	2309.07
45.14	80	603.19	1206.37	1809.56	2412.74	3015.93
50.78	90	763.41	1526.81	2290.22	3053.63	3817.04
56.42	100	942.48	1884.96	2827.43	3769.91	4712.39

4.3.1 Calculations for the Air-Cored Coil

There have been numerous attempts to formulate analytical expressions for the self-inductance of circular air-cored coils, however one of the most elaborate approaches is of Grover. More specifically, in the chapter "Self-inductance of Circular Coils of Rectangular Cross Section"^{11(pp94–113)}, Grover includes formulas for various coil configurations, including coils of square cross section, Brooks coils, and coils of cross section of any desired proportions. The latter configuration is the one of special interest, since the freedom to input a vast range of values is enabling in realizing the golden ratio in this problem. Grover has subcategorized this configuration into two types, one of thin coils (coils approximating solenoids) and one of thick coils (coils approximating a pancake form). For the evaluation of the self-inductance, the reader is directed to various tables, with constants corresponding to dimensional ratios, to act as factors in the actual equation of the self-inductance which also includes N and a . More specifically, the formula (in metric units) for a thin coil is^{11(p105)}

$$L = 0.019739 \frac{2a}{b} N^2 a_{cm} K' \quad (4.24)$$

where quantity K' is the difference of $(K - k)$. K is a function of $2a/b$ (or $b/2a$) and k is a function of $c/2a$ and c/b (or b/c). The formula for a coil approximating pancake form is^{11(p105)}

$$L = 0.001 N^2 a_{cm} P' \quad (4.25)$$

where quantity P' is the product of P and F . P is a function of $c/2a$ and F is a function of $c/2a$ and c/b (or b/c). Therefore, for a coil of dimensions $N_b = 50$, $N_c = 5$, $a_{cm} = 1.0 + (c/2)$:

$$b = 50 \text{ layers} \times 1.024 \text{ mm} = 51.2 \text{ mm}$$

$$c = 5 \text{ layers} \times 1.024 \text{ mm} = 5.12 \text{ mm}$$

$$a_{cm} = 1.0 + \frac{0.512}{2} = 1.256 \text{ cm}$$

$$N = 50 \times 5 = 250 \text{ turns}$$

By inspecting the appropriate dimensional ratio tables (Table 22^{11(p106)}, Table 36^{11(p144)}):

$$\begin{cases} \frac{c}{2a} = 0.2038 \\ \frac{c}{b} = 0.1 \end{cases} \quad k = 0.1170$$

$$\left\{ \frac{2a}{b} = 0.49 \quad K = 0.821211 \right.$$

$$K' = K - k = 0.704211$$

Applying to Equation 4.24, one yields the result of $535 \mu\text{H}$. By observation of the same Equation it is seen that N is of prime importance, since it has a non-linear contribution to the final result. It was found, after experimenting with various inputs, that increasing c while keeping b constant will dramatically increase L and increasing b while keeping c constant will dramatically decrease it. This is due to the concentration and separation of the turns in the axial dimension respectively^{11(p105)}.

4.3.2 FEMM Simulation

In order to alleviate the tediousness of manual calculations, FEMM was employed. FEMM stands for Finite Element Method Magnetics and it is being developed by Dr. David Meeker.¹² It supports scripting in the LUA language¹³ and thus is ideal for automating procedures, such as creating a mesh based on pre-allocated dimensions and then incrementally modifying its elements/groups, extracting data such as inductance and resistance for each configuration. A script was written to sweep through the mean radius a and axial lengths b , as well as radial thickness c , and can be found in the Appendix. The output data file was then formatted in Microsoft Excel, and plots of inductance and resistance vs. axial and radial dimensions were rendered, presented in Figures 4.5 and 4.6.

However, to substantiate the use and validity of the FEMM output, a mesh was created for the same coil configuration as in the previous section. This procedure was generally based on the approach followed in Meeker's magnetostatic tutorial.¹⁴ First, the problem was defined as axisymmetric at d.c. frequency (Figure 4.4(c)). Then, materials were added to the mesh, more specifically *air* and magnet wire *AWG 18* (Figure 4.4(d)). Then, a circuit was created in order to input an arbitrary current of 1 A (Figure 4.4(f)). Finally, the boundary was constrained to a 0 magnetic vector potential (Figure 4.4(e)) and the analysis module was run (Figure 4.4(b)). The analysis yielded a result of $559 \mu\text{H}$, very close to the result obtained from Equation 4.24, with an error of 4.5%, that can be accounted to the approximate nature of the analytical equations in contrast to the accurate approach of the finite element method.

To substantiate the choices made in setting up the mesh, some explanations are necessary: since the entire problem is composed of linear material (copper wire), the inductance does not vary with current amplitude, so that any arbitrary current injection is acceptable, so that $L = \Phi/I$. However, in case there is non-linear materials present (such as a magnetic core), saturation will make the relationship between current and flux non-linear at high current levels. Since most magnetic materials saturate at high field intensities (in the order of Teslas), saturation is of no concern in this particular application, where the field will range from approximately 20 to $100 \mu\text{T}$. Another important point to note is that inductance can have a frequency dependence due to eddy current effects, however

for this problem, they are assumed to be negligible.

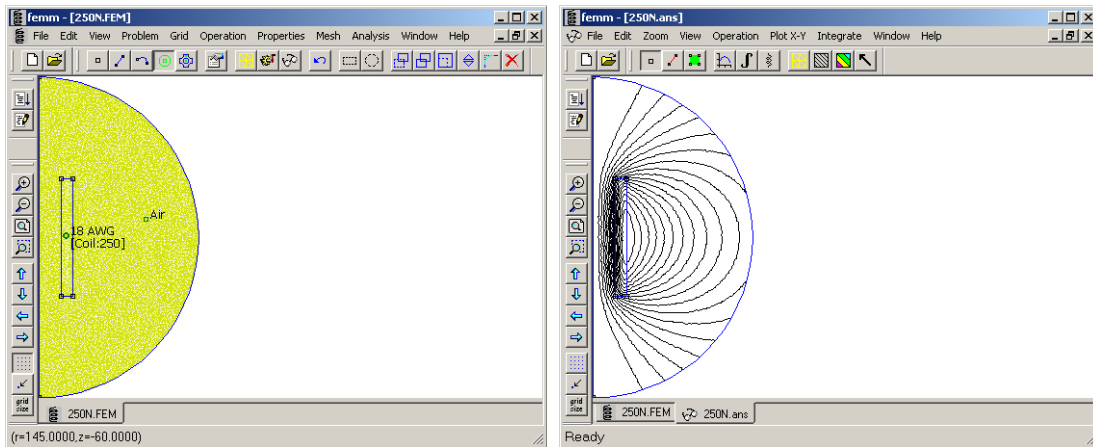
By inspecting the plots of Figure 4.5, one can conclude that indeed the concentration of the turns in the radial dimension leads to an abrupt increase in inductance. Thus, it is a logical decision to confine the choice of coil dimensions even further by selecting a specific radial coil thickness, namely that of 5 layers, displayed in Figure 4.5(a). Also, resistance only varies as a function of N , a and c , however the variation of c has a negligible effect for small layer thicknesses, as the plots of Figure 4.6.

Still, the decision to choose $N_c = 5$ is only one of the many possible coil parameters; the axial number of turns (or axial length) is now a parameter that has to be confronted. However, the output voltage and current, therefore power, of an *air*-cored coil is insufficient for this application; To concentrate the flux lines and thus maximize the power output, a magnetic core will be used, and it is assumed to occupy the entire volume enclosed by the coil.

4.4 Apparent Power Output

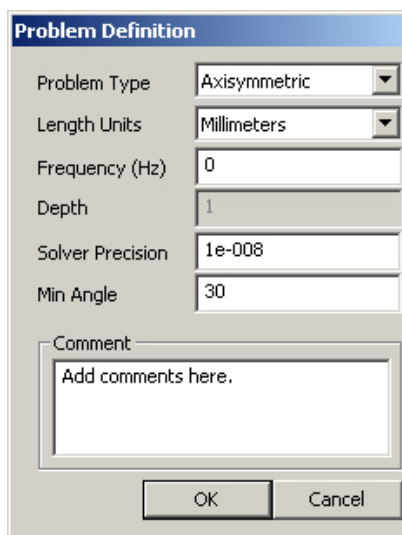
With knowledge of the inductance values of an air-cored coil, a magnetic core may now be included. The air-cored inductance will be multiplied by the constant μ_r , to yield the inductance of a coil with a magnetic core occupying its interior volume. However, before the materials are assessed to deduce their respective permeabilities, the range of field magnitudes have to be looked into. Under a field of $20 \mu\text{T}$ in air, H will be $B/\mu_0 = 20 \times 10^{-6}/4\pi \times 10^{-7} = 15.9 \text{ Am}^{-1}$. Under a field of $100 \mu\text{T}$ in air, H will be $B/\mu_0 = 100 \times 10^{-6}/4\pi \times 10^{-7} = 79.5 \text{ Am}^{-1}$. Therefore, with H ranging from 15.9 to 79.5 Am^{-1} , B-H curves of various materials can be examined to deduce a linear value for μ_r . A material of relative permeability of approximately 5000 at that magnitude of H is Silicon Iron, and many variations of this material exist, having a lower or higher value of μ_r ; The B-H curve of Carpenter Silicon Iron Anneal 1000° is presented in Figure 4.7, which was plotted from the data found in the FEMM 4.0 Materials Library.¹⁵ More specifically, to deduce a value for μ_r from Figure 4.7: At $H = 79.5 \text{ Am}^{-1}$, the corresponding value for B is roughly 0.75 T . This will yield $\mu_r = B/\mu_0 H \approx 7460$. At $H = 30 \text{ Am}^{-1}$ the corresponding value for B is roughly 0.1 T . This will yield $\mu_r = B/\mu_0 H \approx 2652$. An approximately average value of 5000 was chosen, to accommodate all situations and for simplicity. Although the value of 5000 is, as seen, for the most part achievable, 30000 is used purely as a guideline, to aid in exploring the effect of varying μ_r has on the output power. For different applications and/or power requirements, one can assume materials of high permeabilities and -unavoidably- costs.

Equations 4.11, 4.21 and 4.22 were formulated in Microsoft Excel to produce tables of RMS induced voltage, current and load voltage, in order to then retrieve the RMS apparent power values. Plots for the RMS apparent power through the short-circuited coil (with $\vec{Z}_L = 0$) are found in Figures 4.9(a), 4.9(b), and plots for the RMS apparent power through a purely resistive load ($\vec{Z}_L = 10 \Omega$) are found in 4.10(a), 4.10(b). Furthermore, to explore the effects of a load of $\vec{Z}_L = 30 \text{ k}\Omega$ (which is equal to $|\vec{Z}_C|$ of a coil of 500 turns, $a = 56.4 \text{ mm}$ and $c = 5.12 \text{ mm}$), plots for the RMS apparent power through it are found in Figures 4.11(a), 4.11(b). In these plots, the coil

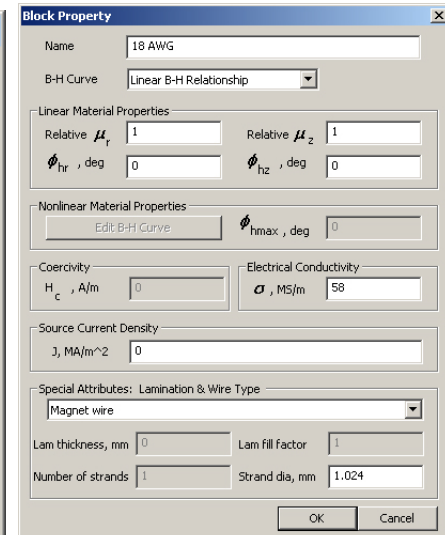


(a) FEMM pre-processor.

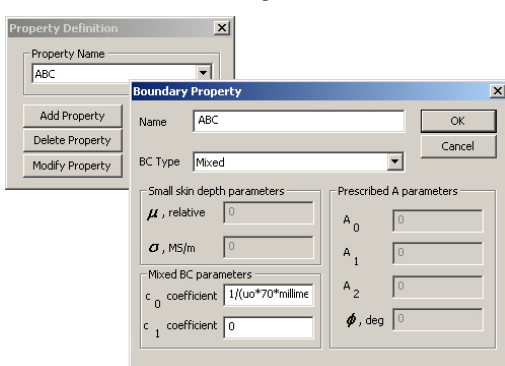
(b) FEMM post-processor.



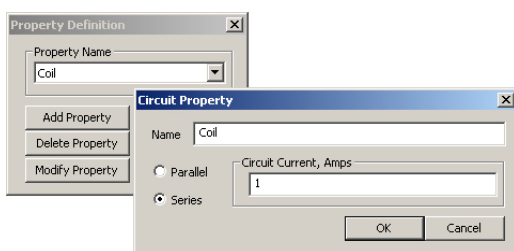
(c) FEMM problem definition.



(d) FEMM material definition.



(e) FEMM boundary definition.



(f) FEMM circuit definition.

Figure 4.4: Mesh creation and analysis modules in FEMM.

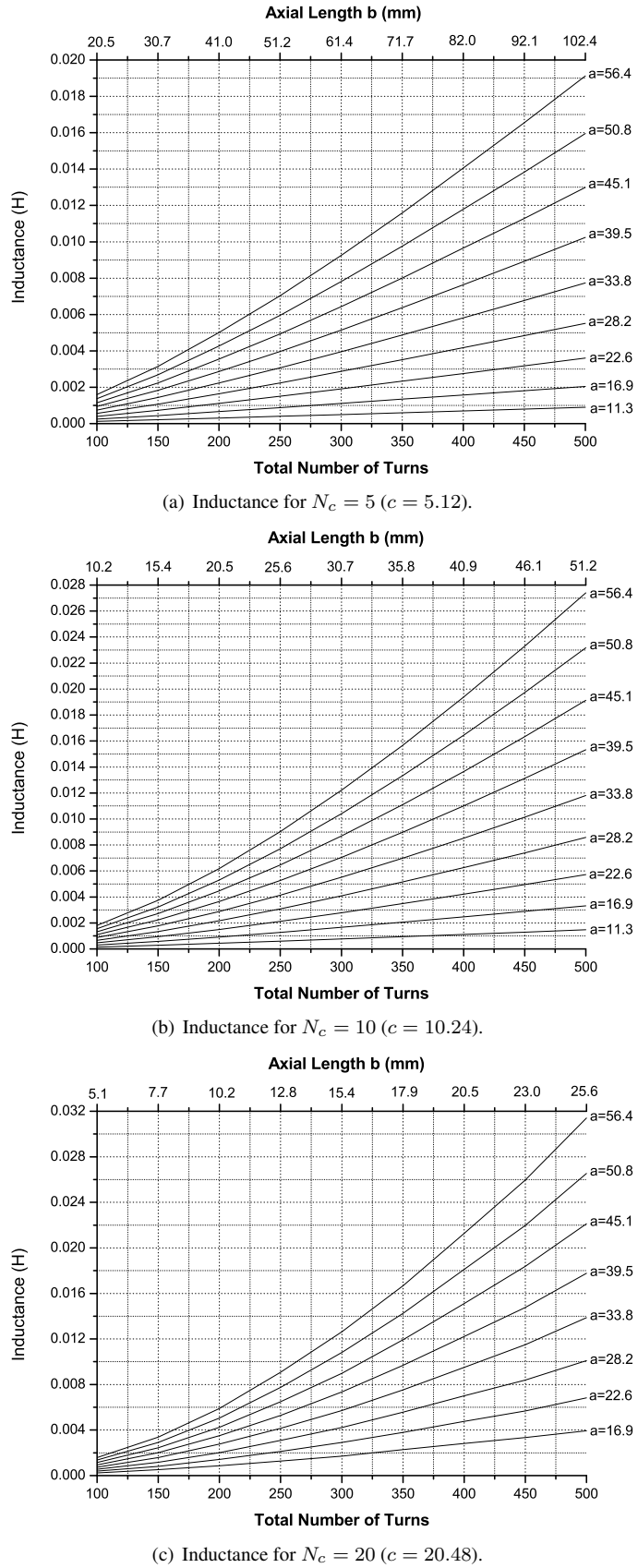


Figure 4.5: Inductance curves for varied mean radius a . Number of radial winding layers N_c and consequently radial thickness c varies for each plot. Thus, total number of turns N corresponds to different axial lengths b and therefore number of axial winding layers N_b . Note that copper wire of thickness AWG 18 (1.024 mm) is used throughout, and values for a , b and c are quoted in mm.

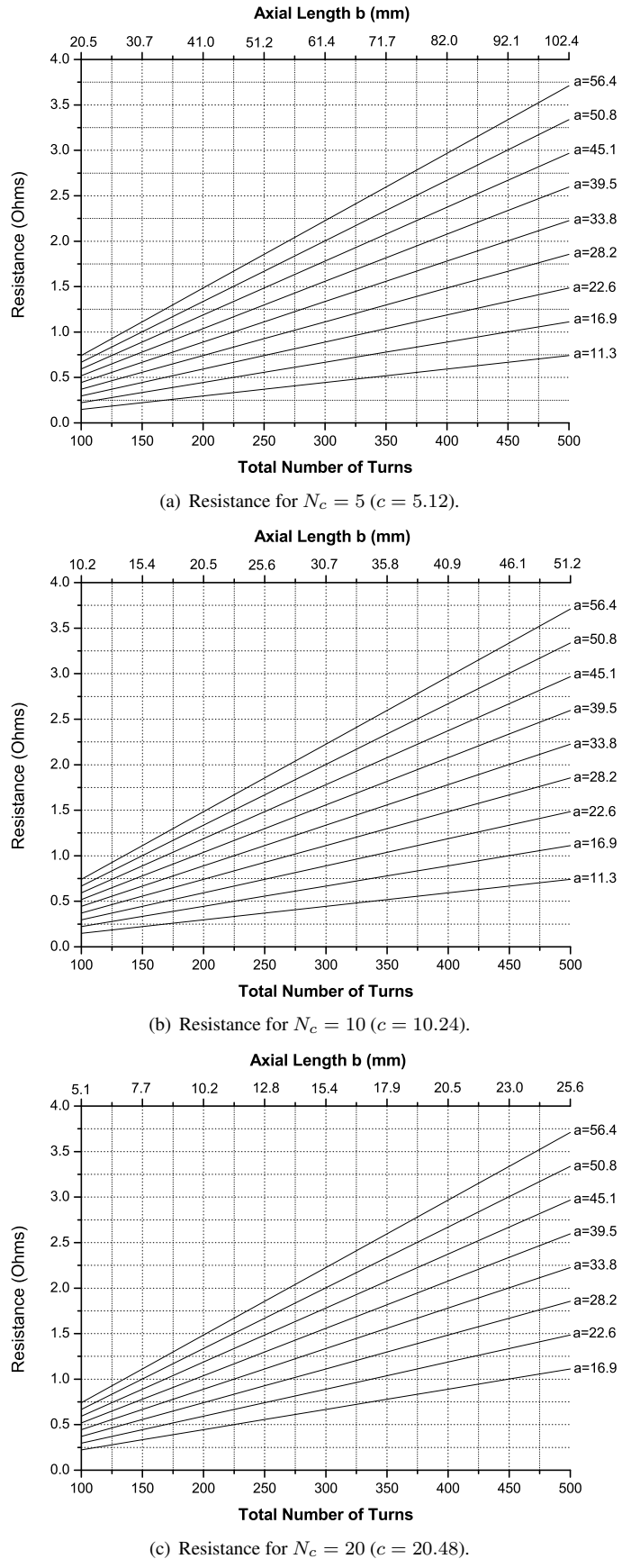


Figure 4.6: Resistance curves for varied mean radius a . Number of radial winding layers N_c and consequently radial thickness c varies for each plot. Thus, total number of turns N corresponds to different axial lengths b and therefore number of axial winding layers N_b . Note that copper wire of thickness AWG 18 (1.024 mm) is used throughout, and values for a , b and c are quoted in mm.

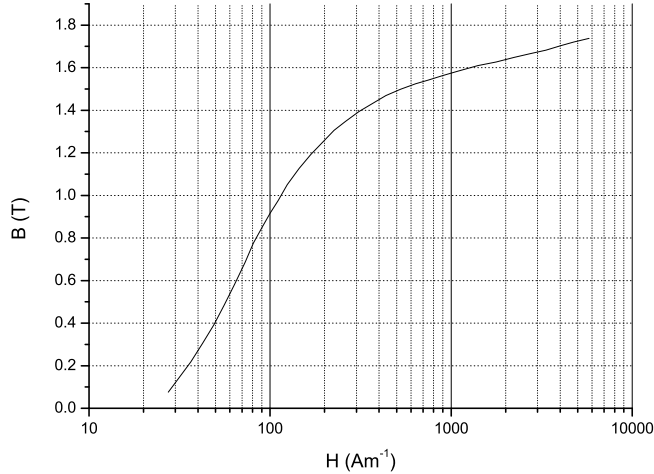
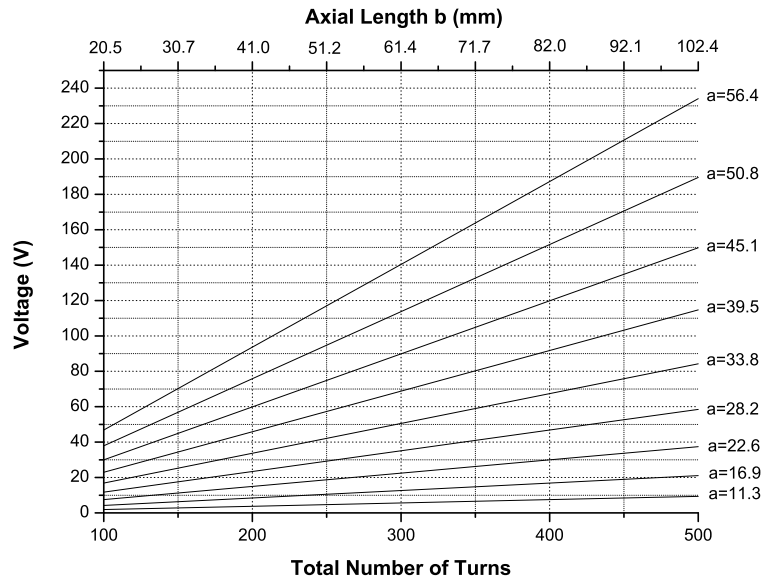


Figure 4.7: B-H curve (log. scale) for Carpenter Silicon Iron Anneal 1000°.¹⁵

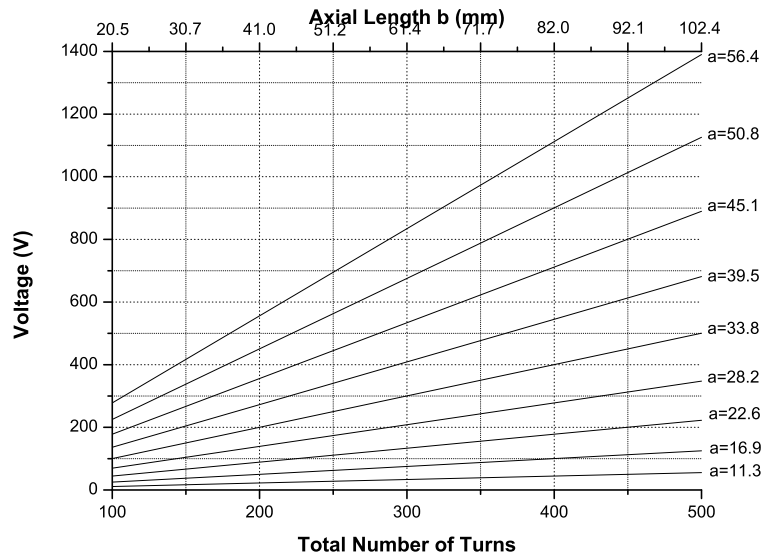
is placed in a field of $30 \mu T$; from the contour plots of Figure 3.4, this corresponds to an average quantity at a vertical distance of 2.7 metres from the conductors; considering when $I = 100 A$, $\mathbf{B} \approx 5 \mu T$ and when $I = 500 A$, $\mathbf{B} \approx 40 \mu T$ and when $I = 1000 A$, $\mathbf{B} \approx 50 \mu T$, the previous quantity of $30 \mu T$ makes sense, since a high conductor current flow is likely to last less (compared to low and medium) over a day.

By examination of the aforementioned plots, it is clear that even the RMS apparent power through the load is much less than the RMS apparent power through the short-circuited coil for the same coil configuration. This can be attributed to Equation 4.22, which indicates that the smaller the ratio of \vec{Z}_L to \vec{Z}_C , the less the voltage drop \vec{V}_L across the load, thus the less the RMS apparent power flowing to the load.

With these thoughts in mind and by looking at the relevant plots, one conclusion that can be drawn regarding the factors affecting the RMS power output of the coil, is that the core material is of very high importance. By inspection of Equation 4.23, one can deduce that the higher the value of μ_r , the higher the induced voltage; however, the inductive reactance $j\omega L$ of the coil is also magnified by that constant, leading to a highly reactive power output. The real power through the load is reduced to a minimum, not only due to the voltage and current having a large difference in phase, but also due to the ratio of \vec{Z}_C to \vec{Z}_L . For maximum power transfer to occur, both \vec{Z}_C and \vec{Z}_L have to be matched, with compromises to be made: either μ_r is reduced to the extreme (by the absence of the magnetic core), leading to a decreased reactance as well as decreased induced voltage, ultimately minimizing the power; or, capacitive compensation is introduced, in order to cancel out the inductive reactance the core brings about, although the effects of that have to be analyzed further. However, the latter seems to be more promising. Simulating the circuit as individual components is therefore crucial in developing a better understanding of the circuit.

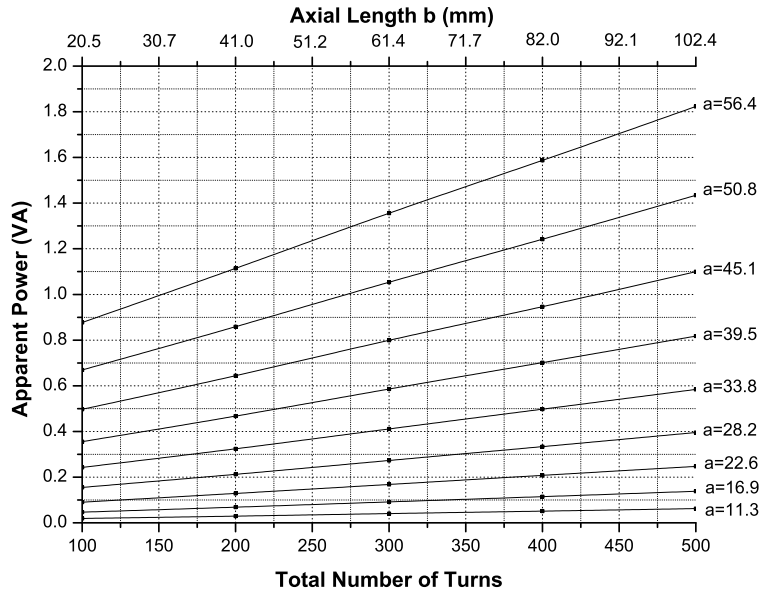


(a) Voltage E induced in the coil for $N_c = 5$ ($c = 5.12$) with a core of $\mu_r = 5000$.

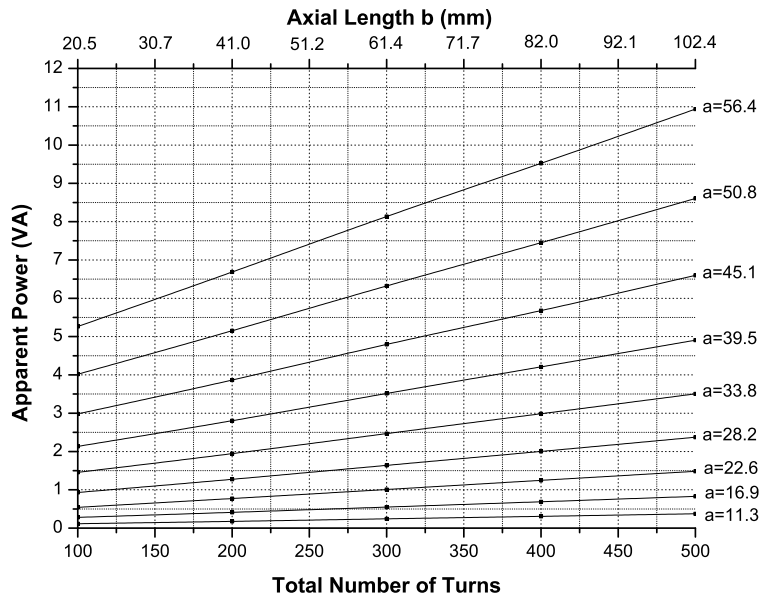


(b) Voltage E induced in the coil for $N_c = 5$ ($c = 5.12$) with a core of $\mu_r = 30000$.

Figure 4.8: Voltage curves for varied mean radius a and axial length b , for a coil of $N_c = 5$ ($c = 5.12$) with cores of varied magnetic permeabilities placed in a field of $30 \mu T$ in air.

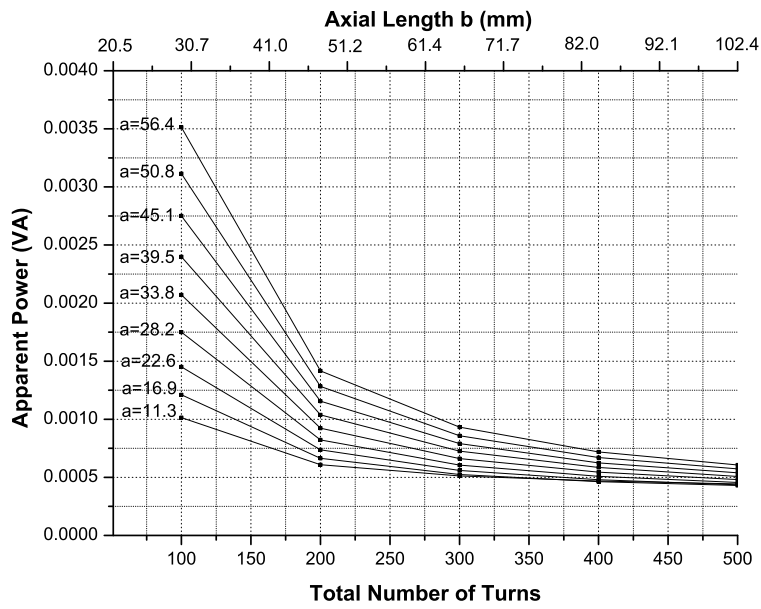


(a) Apparent power through the coil for $N_c = 5$ ($c = 5.12$) with a core of $\mu_r = 5000$, without load.

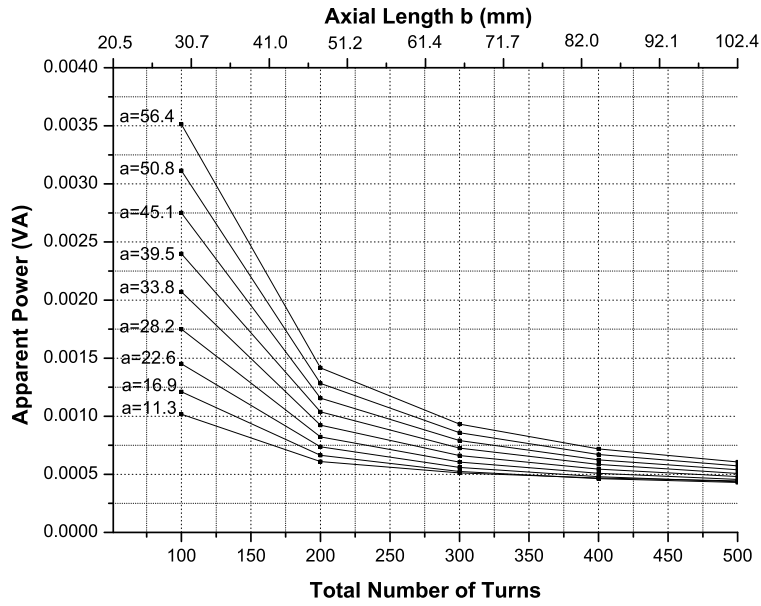


(b) Apparent power through the coil for $N_c = 5$ ($c = 5.12$) with a core of $\mu_r = 30000$, without load.

Figure 4.9: Apparent power curves for varied mean radius a (mm) and axial length b , for a coil of $N_c = 5$ ($c = 5.12$) with cores of varied magnetic permeabilities, with $\vec{Z}_L = 0$, placed in a field of $30 \mu T$ in air.

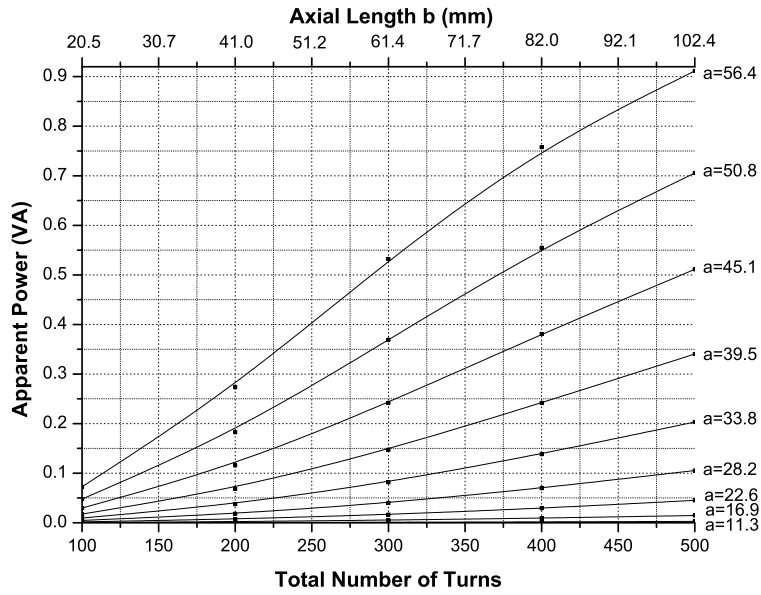


(a) Apparent power through a 10Ω load for $N_c = 5$ ($c = 5.12$) with a core of $\mu_r = 5000$.

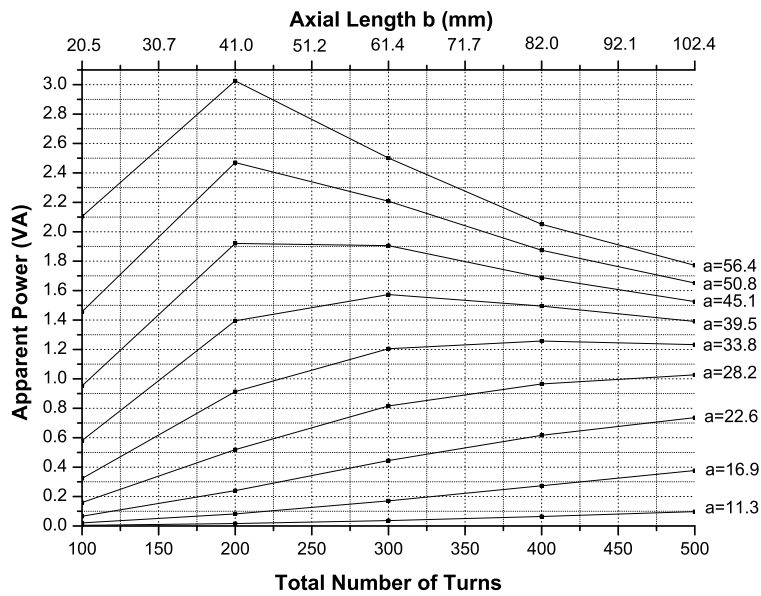


(b) Apparent power through a 10Ω load for $N_c = 5$ ($c = 5.12$) with a core of $\mu_r = 30000$.

Figure 4.10: Apparent power curves for varied mean radius a (mm) and axial length b , for a coil of $N_c = 5$ ($c = 5.12$) with cores of varied magnetic permeabilities, with $Z_L = 10 \Omega$, placed in a field of $30 \mu T$ in air.



(a) Apparent power through a $30 \text{ k}\Omega$ load for $N_c = 5$ ($c = 5.12$) with a core of $\mu_r = 5000$.



(b) Apparent power through a $30 \text{ k}\Omega$ load for $N_c = 5$ ($c = 5.12$) with a core of $\mu_r = 30000$.

Figure 4.11: Apparent power curves for varied mean radius a (mm) and axial length b , for a coil of $N_c = 5$ ($c = 5.12$) with cores of varied magnetic permeabilities, with $\vec{Z}_L = 30 \text{ k}\Omega$, placed in a field of $30 \mu\text{T}$ in air.

Chapter 5

Circuit Simulation

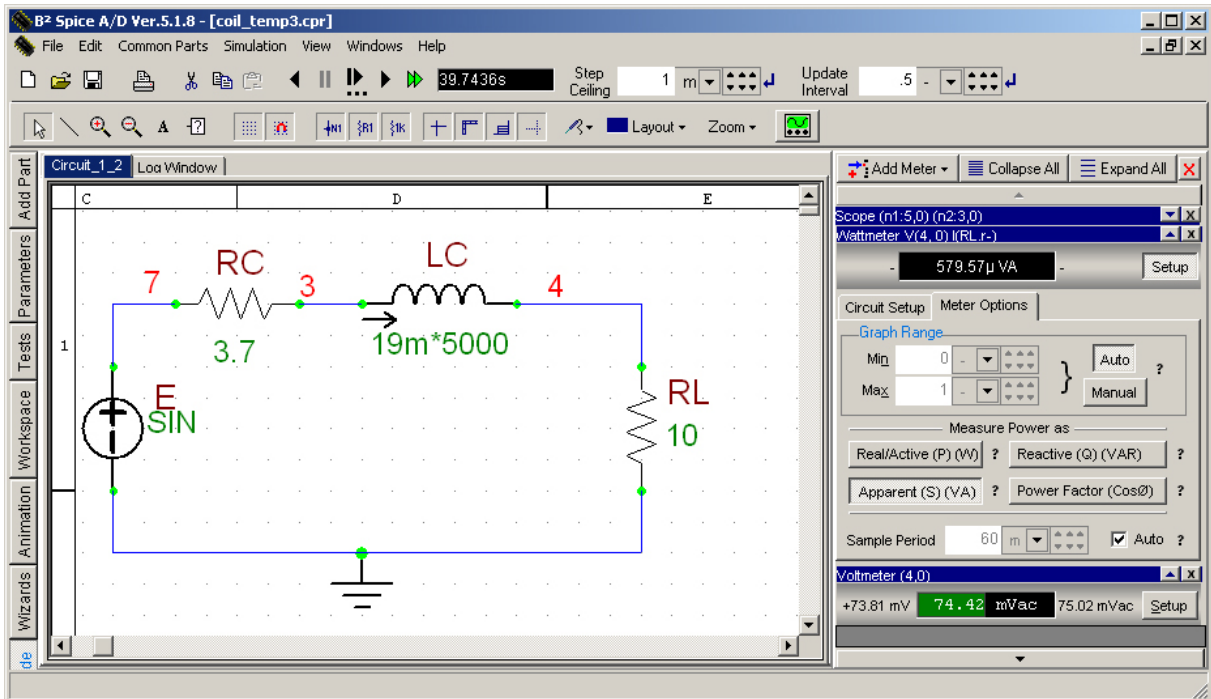


Figure 5.1: B2Spice simulation results for the apparent power and voltage through a $10\ \Omega$ load for $N_c = 5$ ($c = 5.12$) with a core of $\mu_r = 5000$. The circuit is consistent with Figure 4.3, without the conditioning circuit.

The circuit depicted in Figure 4.3 has to be simulated, in order to deduce results, to verify the results yielded from the circuit equations. However, due to the variety of conditioning/control circuits available, the first attempt will consider the absence of the intermediate block diagram, thus connecting nodes a with c' , and b with d' . The chosen coil configuration is of $N = 500$, $N_c = 5$, $N_b = 20$, $a = 56\ \text{mm}$, $\mu_r = 5000$. That results to $R_C = 3.7\ \Omega$ and $L_C \times \mu_r = 19 \times 10^{-3} \times 5000 = 95\ \text{H}$. The signal source holds a value of $E = 230 \times \sqrt{2} = 327\ V_p$, which approximately corresponds to a field of $30\ \mu\text{T}$. Also, the source is sinusoidal and of frequency $50\ \text{Hz}$: the superposition of waveforms of arbitrary magnitudes and phases will be sinusoidal, if the frequency of each field is identical, such as in this case. This circuit data was used to design a schematic in B2Spice,¹⁶ with all components

represented by their ideal equivalents. A wattmeter and voltmeter are included in the simulation, such as in Figure ??, which is a screenshot of the B2Spice simulation. The data extracted from the simulation agrees to a great extent with the results shown in Figure 4.10. That meaning, however, that the problem of making all the potential power available to a load still exists. More specifically, the window displays a load voltage $V_L = 74.42 \text{ mV}_p$ and an apparent power $P_L = 579.57 \mu\text{VA}$. From Figure 4.11 it can be observed that the apparent power through the load will increase, since the coil and load are matched. The spice simulation was repeated with a load of $30 \text{ k}\Omega$, yielding a load voltage $V_L = 160 \text{ V}_p$ and an apparent power of 0.862 VA , very close to the results of Figure 4.11.

Chapter 6

Conclusions

The immediate conclusions one can draw is that this type of scavenging mechanism is able to provide a very high voltage with a very low current, due to the high impedance created by the essential function of the mechanism itself, the self-inductance. As seen in subsection 4.3.2, inductance rises dramatically as radial thickness increases; still, the total number of turns have a substantial (linear) contribution to the voltage induced in the coil, as seen by Equation 4.11, therefore axial length of the coil then becomes a practical concern, since it needs to be increased for the coil to achieve the same total number of turns. Also, the magnetic core is non-linear, and although it has been approximated to be linear at a specific interval, there will be deviations in the value of μ_r for fields higher than $30\mu T$. Also, mutual inductance is ignored, since due to the coil's dimensions and positioning it was assumed to be negligible. However, if the coil were to be placed in the immediate vicinity of the conductors, one would have to consider its effects. In this case, it will tend to oppose the induced voltage.

Figure 4.10 reveals that the transferred power is very low for a non-matched load, while following a downward trend as N increases. Furthermore, from Figure 4.11(b) it can be seen that even when the coil and load are approximately matched, there is some point for a coil of larger mean radius a at which power transferred to the load will follow a downward trend, due to increase in inductance of the turns and the effect of a very high permeability core. Therefore, one can deduce the 'golden ratio' physical configuration for the coil, by selecting a core of medium permeability and appropriate axial and radial dimensions.

6.1 Future work

6.1.1 Coil Design Revision

A matter that was dealt with seriously in Chapter 4 is the resistance of the turns of the coil. It seems now that minimizing it (by selecting a wire of diameter 1.024 mm, AWG 18) should not be emphasized on much, since the resistance is overshadowed by the inductive reactance; the effect of the magnetic core is so noticeable that one could maybe even *neglect* the resistance of the turns when considering \vec{Z}_L . Having that in mind, a wire type of

smaller diameter can be chosen, to physically shrink the coil's dimensions, especially the axial length, on which this change would be more noticeable than on the radial thickness, as there are more axial than radial turns.

Also, another practical concern that will arise problems in the application of the coil is the induced voltage. From the voltage tables, it can be seen that voltage levels as a function of the coil dimensions and core permeability, are very high; this will be a major issue when designing an appropriate conditioning circuit, since the voltage will need to be scaled down substantially until a suitable, for the load, level is reached. For an array of coils connected in parallel, the currents would add up while the induced voltages would be approximately the same if the coils were to be placed in the vicinity of each other. This would allow minimizing the coil dimensions, while maximizing the output power. This concept, of course, needs to be reviewed and evaluated.

Also, a crucial matter is the selection of the core. A review of the all current material permeabilities is necessary. Also, when building the final design, two issues that will prevail are the shapes in which those materials come in (laminated shapes etc.) and their costs. After all, if the cost of realizing such a scavenging mechanism are too high, it would be wiser to look into other methods of powering a wireless sensor.

After an acceptable design is achieved (square or circular coil), the best approach would be to build the coil and test it by measuring the induced voltage and current without a load connected, if not in a substation environment of the configurations assumed in Section 3.4.1, in a field of known magnitude (previously calculated via the matlab algorithm). Then, one could compare the experimental data to the theoretical data and arrive at conclusions that would dictate whether or not the methods used need revising.

6.1.2 Conditioning Requirements

A control/conditioning circuit interconnected to the source and load as pictured by Figure 4.3 is a diverse and extensive subject that will need a substantial amount of dedication. A few observations, that will facilitate future work, need to be made: the first observation regarding the waveform across nodes *a* and *b* in the circuit of Figure 4.3 is that it is sinusoidal. The sinusoidal waveform, therefore, needs to be converted into a DC voltage in order to 'feed' the device. The second observation is that although the currents in the overhead conductors are a pure 50 Hz sinusoid, in practice there will certainly be deviations at times, resulting in harmonic content in the waveform. With the inclusion of a rectifier circuit, a harmonically distorted waveform can be converted to DC, since that circuit is essentially a low pass filter with a very steep roll-off. In any case though, there will be losses. However, that is only one small part of the conditioning circuit.

The power transferred to the load is a principal matter. In the present study it has been assumed that the load impedance \bar{Z}_C only contains a real part, namely a resistive component. However, in a practical situation, the impedance of a wireless sensor will contain a reactive component, and its magnitude will depend on the design of that particular sensor. Furthermore, the load most probably will not be linear; a device which implements integrated circuits that process data and transfer it wirelessly will vary its impedance, depending on the amount of calculations it is carrying out every instant, on the transmission distance and data rate. The IEEE 802.15.4 ZigBee

technology is now the most promising one in terms of efficient power consumption. This lies in the fact that active or 'sleep' mode is used in this technology. When in active mode, a module of such kind can consume as low as 14.7 mA in receive mode and 15.7 mA in transmit mode operating on a supply voltage varying between 1.8 V and 3.6 V. When in 'sleep' mode, and depending on the software the sensor utilises, power consumption drops to the μ W range.¹⁷ However, as previously, additional circuitry such as the processing module will require further power to operate, depending on the choice of integrated circuits and the software employed.

For maximum power transfer, $\vec{Z}_C = \vec{Z}_L^*$. Since the load will most probably be non-linear, and the coil impedance is assumed to be linear in the range of field magnitudes considered in this study, the conditioning circuit that mediates between the coil and the load, will have to perform the function of matching \vec{Z}_C and \vec{Z}_L at all times. That means that once a final design for the coil is reached and the load characteristics are known, the conditioning circuit can be designed based on the characteristics of the load and the range of field magnitudes the coil will experience.

Also, since the currents in the overhead conductors will vary, the field may not be adequate for powering the load directly at all times. Therefore, it would be wise to include a battery charging module in the control/conditioning circuit. However, the previously mentioned control/conditioning circuit still applies, since the current and voltage levels a charging module can handle depend on the charging module and the battery material themselves.

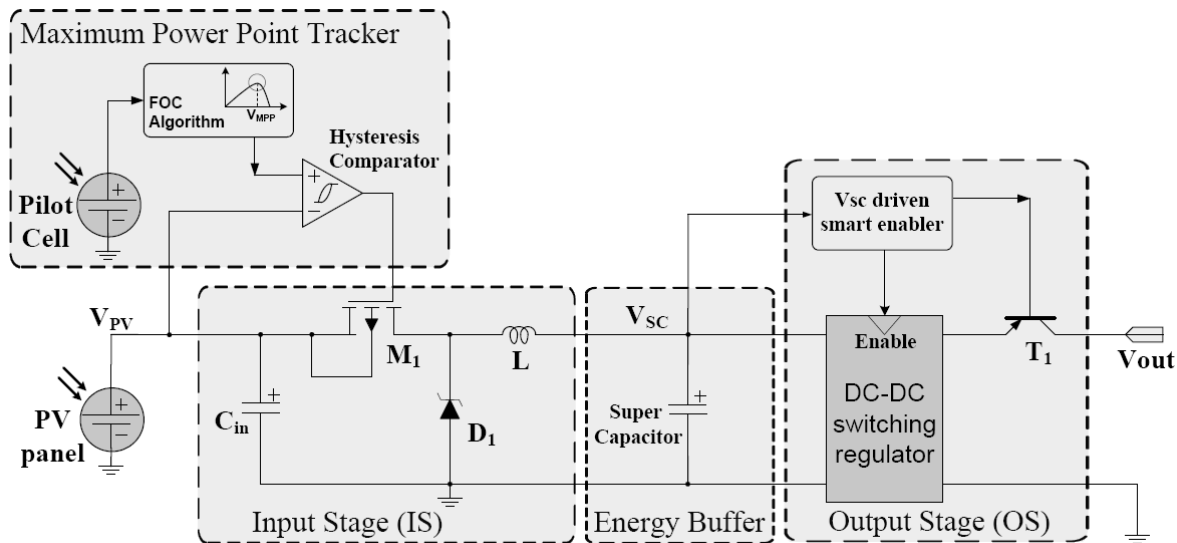


Figure 6.1: Solar Harvester circuit schematic.²

Dondi et al.² have devised a schematic (Figure 6.1), which employs three different stages. The input stage, which accumulates the energy collected from the PV panel into a supercapacitor, is designed as a DC-DC converter. A pulse width modulated signal generated by a controller stabilizes the voltage. The desired voltage is a function of the power collected from the PV panel and the charge state of the supercapacitor. A Maximum Power Point Tracker collects the maximum power available from the PV panel, by controlling the switching operation. An Output Stage Regulator implements an output DC-DC regulator and a control circuit which enables the output

stage only when the DC-DC converter can operate efficiently.

A similar schematic can be employed for charging a supercapacitor via the induction coil. The control circuit could possibly employ a hysteresis comparator to switch between powering the load directly or charging the battery.¹⁸ Although, the DC-DC converter would be replaced by an AC-DC converter. Furthermore, the electronic components employed in this schematic would have to be replaced accordingly, to suit the power output of the coil and the power consumption characteristics of the load. However, the possibility of powering a wireless sensor via electromagnetic induction in the environment of a substation *is* feasible, with knowledge of the load characteristics and if one devises an appropriate conditioning circuit.

Acknowledgements

I would like to thank the following people:

my project supervisor, Dr. Noureddine Harid, for his participation, time and patience

Alex Bogias, for his help

Dr. Mehrdad Ghassempoory, for his advice on typesetting with L^AT_EX

Dr. David Meeker, for replying to my e-mails on FEMM

and

the staff at AREVA, for answering my phonecall regarding SLIM

Bibliography

- [1] THOMAS J., QIDWAI M. and KELLOGG J. Energy Scavenging for Small-Scale Unmanned Systems. *Journal of Power Sources*, 2006, **159**, 1494–1509.
- [2] DONDI D., BERTACCHINI A., LARCHER L., PAVAN P., BRUNELLI D. and BENINI L. A Solar Energy Harvesting Circuit for Low Power Applications. *ICSET 2008*.
- [3] ZHU M., REID A., FINNEY S. and JUDD M. Energy Scavenging Technique for Powering Wireless Sensors. *International Conference on Condition Monitoring and Diagnosis, Beijing, China*, 2008.
- [4] GRIFFITHS D.J. *Introduction to Electrodynamics*, 3rd Edition. Prentice Hall of India Private Limited, 2002.
- [5] GRANT I. and PHILIPS W. *Electromagnetism*, 2nd Edition. John Wiley & Sons, Chisester, England, 1990.
- [6] MORO F. and TURRI R. Analytical Calculation of the Environmental Magnetic Field Generated by Single and Double Circuit Power Lines. *XVth International Symposium on High Voltage Engineering*, 2007.
- [7] STEVENSON W.D. *Elements of Power System Analysis*, 4th Edition. McGraw-Hill, Singapore, 1982.
- [8] Areva T&D Technology Centre, St. Leonards Works, St Leonards Avenue, Stafford, England. *SLIM Electromagnetic Engineering 3.7.1 User Manual*, 2004.
- [9] Mathworks Corporation, Natick, Massachussets, U.S.A. *MATLAB R2007b*, 2007.
- [10] Microsoft Corporation. *Microsoft Office Excel 2003*, 2003.
- [11] GROVER F. *Inductance Calculations*. Dover Publications, New York, N.Y., 1973.
- [12] MEEKER D. *FEMM 4.0 Manual*, 2006. [Accessed 16th Feb 2009].
Available from: <http://femm.foster-miller.net/Archives/doc/manual.pdf>
- [13] DE FIGUEIREDO L., CELES W. and IERUSALIMSCHY R. *LUA 4.0 Scripting Language*. Computer Science Department, Pontifícia Universidade Católica, Rio de Janeiro, Brasil, 2000. [Accessed 16th Feb 2009].
Available from: <http://www.tecgraf.puc-rio.br/lua/>

- [14] MEEKER D.C. *FEMM 4.0 Magnetostatics Tutorial*, 2004. [Accessed 29th Feb 2009].
Available from: <http://femm.foster-miller.net/Archives/doc/tutorial-magnetic.pdf>
- [15] MEEKER D.C. Finite Element Method Magnetics v4.0.1 (*03Dec2006 Build*). [Accessed 25th Feb 2009].
Available from: <http://femm.foster-miller.net>
- [16] Beige Bag Software, Ann Arbor, Minnesota, U.S.A. *B2 Spice A/D v4 Lite*, 2007.
- [17] KLUGE W., POEGEL F., ROLLER H., LANGE M., FERCHLAND T., DATHE L. and EGGERT D. A Fully Integrated 2.4-GHz IEEE 802.15.4-Compliant Transceiver for ZigBee Applications. *IEEE Journal of Solid-State Circuits*, 2006, **41**, no. 12, 2767–2775.
- [18] CUADRAS A., AMOR N.B. and KANOUN O. Smart Interfaces for Low Power Energy Harvesting Systems. In *IMTC 2008 - IEEE International Instrumentation and Measurement Technology Conference*, Victoria, Vancouver Island, Canada, 2008.

Appendix

Matlab code:

```
1 %-----  
2 %-----Magnetic Field Analysis-----  
3 %-----by Orpheas Kypris-----  
4 %-----BEng Electrical & Electronic, Cardiff University-----  
5 %-----  
6 close all;  
7 clear all;  
8 syms x;  
9 syms y;  
10 %-----  
11 %-----Change any of these variables! -----  
12 %-----  
13 %-----  
14 %define RMS current in overhead conductors  
15 I=1000;  
16 %define calculation range (horizontal and vertical axes)  
17 x1=-9;  
18 x2=9;  
19 y1=3;  
20 y2=-6;  
21 %define left and right conductor coordinates relative to origin (middle  
22 %conductor)  
23 x_displ=3; %left conductor is displaced "x_displ" metres towards left  
24 y_displ=0; %left conductor is displaced "y_displ" metres towards ground  
25 x_disp2=-3; %right conductor is displaced "x_displ" metres towards left  
26 y_disp2=0; %right conductor is displaced "x_displ" metres towards left  
27  
28 %-----  
29  
30 %-----  
31 %-----MAIN ALGORITHM (alter with caution)-----
```

```

32 %-----
33 %-----
34 %length of axes (for definining matrix later on)
35 range_x=x1:x2;
36 range_y=y1:y2;
37
38 %preallocate matrices according to size of mesh
39 %B_total=zeros(length(range_y)+1,length(range_x)+1);
40 matrix_B1_B2_B3_x=zeros(length(range_y)+1,length(range_x)+1);
41 matrix_B1_B2_B3_y=zeros(length(range_y)+1,length(range_x)+1);
42
43 %definition of sinusoidal 3-phase currents
44 I11=I;
45 I12=I*exp(j*(-(2/3)*pi));
46 I13=I*exp(j*(-(4/3)*pi));
47
48 %loop around, storing x and y field components into matrices
49 incr_y=1;incr_x=1; %dont change these
50
51 for x=x1:0.1:x2 %increment by 0.1 m
52 for y=y1:-0.1:y2
53
54 %define magnitudes of distances from coordinates relative to 0,0 (middle
55 %conductor)
56 r1=[x+x_disp1 y+y_disp1];
57 r2=[x y];
58 r3=[x+x_disp2 y+y_disp2];
59
60 mag1=sqrt(((r1(1))^2)+((r1(2))^2)); %calc distance of point P from
61 %1st conductor using Pythagorean Theorem
62 mag2=sqrt(((r2(1))^2)+((r2(2))^2));
63 mag3=sqrt(((r3(1))^2)+((r3(2))^2));
64
65 %define relative permeability of free space
66 u_nought=4*pi*10^-7;
67
68 %define B-fields in x-direction at point P
69 B1_x=-((u_nought)*(I11)/(2*pi*(mag1)^2))*r1(2);
70 B2_x=-((u_nought)*(I12)/(2*pi*(mag2)^2))*r2(2);
71 B3_x=-((u_nought)*(I13)/(2*pi*(mag3)^2))*r3(2);
72
73 %define B-fields in y-direction at point P
74 B1_y=((u_nought)*(I11)/(2*pi*(mag1)^2))*r1(1);
75 B2_y=((u_nought)*(I12)/(2*pi*(mag2)^2))*r2(1);

```

```

76 B3_y=((u_nought)*(I13)/(2*pi*(mag3)^2))*r3(1);
77
78 %define B-fields in x- and y-direction at point P
79 B1_B2_B3_x=B1_x+B2_x+B3_x;
80 B1_B2_B3_y=B1_y+B2_y+B3_y;
81
82 matrix_B1_B2_B3_x(incr_y,incr_x)=B1_x+B2_x+B3_x;
83 matrix_B1_B2_B3_y(incr_y,incr_x)=B1_y+B2_y+B3_y;
84
85 abs_B1_B2_B3_x=abs(B1_B2_B3_x); %evaluate time modulus
86 abs_B1_B2_B3_y=abs(B1_B2_B3_y);
87
88 %define total B-field at point P
89 new_B_total(incr_y,incr_x)=sqrt((abs_B1_B2_B3_x)^2+(abs_B1_B2_B3_y)^2); %store time modulus
90
91 B_total(incr_y,incr_x)=sqrt((B1_B2_B3_x)^2+(B1_B2_B3_y)^2);
92
93 incr_y=incr_y+1;
94 end
95     incr_x=incr_x+1;
96     incr_y=1;
97 end
98
99 x=x1:0.1:x2;
100 y=y1:-0.1:y2;
101 %create mesh grid
102 [X,Y]=meshgrid(x,y);
103 %-----
104 %-----Plotting Code-----
105 %-----
106 %-----
107 %plot B-fields with respect to heights and x displacement (new graph)
108 %--PLOT 1--
109 subplot(2,2,1)
110 [C,h]=contour3(X,new_B_total,Y,[-1 -1.5 -2 -2.5 -3]);
111 clabel(C,h)
112 xlabel 'x (m)'
113 ylabel 'B (Tesla)'
114 grid on
115 %rotate graph
116 view(0, 90);
117 %autoset y axis limits
118 axis 'auto y'
119

```

```

120 %plot vector field normal to the xy plane (new graph) and also plot contour
121 %lines of B
122 %--PLOT 2--
123 subplot(2,2,2)
124 quiver(x,y,matrix_B1_B2_B3_x,matrix_B1_B2_B3_y,50)
125 hold on
126 [C,h]=contour(X,Y,new_B_total,[0.00006 0.00004 0.00002]);
127 clabel(C,h)
128 xlabel 'x (m)'
129 ylabel 'y (m)'
130 grid on
131
132 %plot contour lines of B
133 subplot(2,2,3)
134 [C,h]=contour(X,Y,new_B_total,[0.0002 0.0001 0.00006 0.00004 0.00003 0.00002]);
135 clabel(C,h)
136 %clabel(C,h,'manual','Fontsize',12)
137 xlabel 'x (m)'
138 ylabel 'y (m)'
139 grid on

```

LUA script for FEMM:

```

1 -----
2 -----FEMM LUA script-----
3 ----- Induction Coil Parametrization -----
4 -----
5 -- This script varies the radial and axial dim --
6 -- ensions of a coil and outputs Inductance an --
7 -- d Resistance to file specified by variable --
8 -- 'outputfile'... --
9 -----
10 -----
11 ---!!!Note: all values are specified in mm!!!---
12 -----
13 -----
14 ----Instructions: Open FEMM, File -> Open Lua Script-----
15 ----The output will by default be written on -----
16 ----'coil_results.txt' in the script directory... -----
17 -----
18 -----
19 -- Initialisation of variables
20 Wire_d = 1.024 --specify wire diameter (remember to modify the according material

```

```

21      --property in FEMM along with this)
22 N_initial = 100 --specify initial total number of turns
23 N_increment = 50 --specify the amount number of turns to increment by
24 Nc = 20 --specify radial number of turns
25 c = Nc * Wire_d
26 Nb_initial = N_initial/Nc --specify initial number of turns along axial dimension b
27 b_initial = Nb_initial * Wire_d --specify initial axial dimension
28 b_increment = (N_increment/Nc) * Wire_d
29 initial_mean_radius = 5.64*3 --5.64 mm for area equivalent to d=0.01 m
30 increment_mean_radius = 5.64
31 initial_inside_radius = initial_mean_radius - (c/2)
32 initial_outside_radius = initial_mean_radius + (c/2)
33 start_time=0
34 outputfile = "coil_results.txt" --file to output results to
35
36 ---build mesh from scratch---
37 newdocument(0);
38
39 mi_probdef(0,'millimeters','axi',1e-8,0,30)
40 mi_addnode(initial_inside_radius,b_initial/2);
41 mi_addnode(initial_outside_radius,b_initial/2);
42 mi_addnode(initial_inside_radius,-b_initial/2);
43 mi_addnode(initial_outside_radius,-b_initial/2);
44
45 mi_addsegment(initial_inside_radius,b_initial/2,initial_outside_radius,b_initial/2);
46 mi_addsegment(initial_outside_radius,b_initial/2,initial_outside_radius,-b_initial/2);
47 mi_addsegment(initial_outside_radius,-b_initial/2,initial_inside_radius,-b_initial/2);
48 mi_addsegment(initial_inside_radius,-b_initial/2,initial_inside_radius,b_initial/2);
49
50 r = 20 * initial_mean_radius;
51 mi_addnode(0,r);
52 mi_addnode(0,-r);
53 mi_addsegment(0,r,0,-r);
54
55 mi_addarc(0,-r,0,r,180,5);
56 mi_addcircprop("Coil",1,1);
57 mi_addblocklabel((initial_inside_radius + initial_outside_radius)/2,0);
58 mi_addblocklabel(0.95*r,0);
59 mi_addmaterial("AWG18",1,1,0,0,58,0,0,0,3,0,0,1,1.024);
60 mi_addmaterial("Air" ,1,1,0,0,0,0,0,1,0,0,0);
61 mi_addboundprop("abc",0,0,0,0,0,1/(r*millimeters*pi*4.e-7),0,2);
62 mi_selectlabel((initial_inside_radius+initial_outside_radius)/2,0);
63 mi_setblockprop("AWG18",0,r/50,"Coil",0,2,N_initial);
64 mi_clearselected();

```

```

65     mi_selectlabel(0.75*r,0);
66     mi_setblockprop("Air",0,r/50,'<None>',0,0,0);
67     mi_clearselected();
68     mi_selectarcsegment(r,0);
69     mi_setarcsegmentprop(5,"abc",0,0);
70     mi_clearselected();
71     mi_selectnode(initial_inside_radius,b_initial/2)
72     mi_selectnode(initial_outside_radius,b_initial/2)
73     mi_setnodeprop("propname",1)
74     mi_clearselected();
75     mi_selectnode(initial_inside_radius,-b_initial/2)
76     mi_selectnode(initial_outside_radius,-b_initial/2)
77     mi_setnodeprop("propname",2)
78     mi_clearselected();
79     mi_saveas('tmp.fem');

80

81 ---create and write file which holds results-----
82

83 handle = openfile(outputfile, "w")      -- overwrite old results file!
84 write(handle, "\nSweeping through coil dimensions (length and radius)\n")
85 write(handle, "Start time: ", start_time, "\n")
86 write(handle, "Coil is 20.48 mm long (b) \n")
87 write(handle, "      5.64 mm inside radius\n" )
88 write(handle, "      5.64 + 5.12 mm outside radius\n" )
89 write(handle, "      Output values correspond to following parameters\n" )
90 write(handle, "      current radius (a) / current length (b) / current number of turns (N) /
91             current axial number of turns (Nb) / current radial number of turns
92             (Nc) / current (I) / resistance (Ohms) / inductance (L)\n" )
93 closefile(handle)
94 end_n = 8 --number of times to loop around changing axial length b
95

96 -- Loop through the radius of coil
97 for i=0,9 do
98     handle = openfile(outputfile,"a")
99     closefile(handle)
100    cur_radius = initial_mean_radius + (increment_mean_radius * i)
101    -- Loop through the length of coil
102    for n=0,end_n do
103        current_N = N_initial + (N_increment * n)
104        current_Nb = current_N/Nc
105        cur_length = b_initial + (b_increment * n)
106
107        mi_selectlabel(cur_radius + 1, 0)
108        mi_setblockprop("AWG18",0,r/50,"Coil",0,2,current_N);

```

```

109     mi_clearselected();
110
111     -- Solve and save results
112     mi_createmesh()
113     mi_analyze()
114     mi_loadsolution()
115
116     current,resistance,inductance = mo_getcircuitproperties('Coil');
117     handle=openfile(outputfile,"a")
118     write(handle,cur_radius, " ", cur_length, " ",current_N, " ", current_Nb, " ",Nc, " ",
119             current, " ", resistance, " ", inductance, "\n")
120     closefile(handle)
121
122     -- Increase length of coil in mesh
123     mi_selectgroup(1)
124     mi_move_translate(0,b_increment/2)
125     mi_selectgroup(2)
126     mi_move_translate(0,-(b_increment/2))
127 end
128
129 --restore coil back to original dimensions so
130 --that looping can start with different radius
131 --but same b next iteration
132     mi_selectgroup(1)
133     mi_move_translate(0,-(end_n+1) * (b_increment/2))
134     mi_selectgroup(2)
135     mi_move_translate(0,(end_n+1) * (b_increment/2))
136
137     -- increase radius by 'increment'
138     mi_selectgroup(1)
139     mi_move_translate(increment_mean_radius,0)
140     mi_selectgroup(2)
141     mi_move_translate(increment_mean_radius,0)
142 end
143
144 -----
145 -- Document the total run time and finish up --
146 -----
147 handle = openfile("outputfile", "a")
148 end_time = date()
149 write(handle, "\nEnd time: ", end_time )
150 closefile(handle)
151
152 messagebox("All done!\n\nStarted " .. start_time .. "\nFinished " .. end_time)

```